# NUMERICAL ANALYSIS OF A FLAPPING ELLIPTIC FLAT PLATE IN HOVER: A STUDY OF THE LEADING EDGE VORTEX DYNAMICS.

by

C. VIVEK NAIR

Presented to the Faculty of the Graduate School of

The University of Texas at Arlington in Partial Fulfillment

of the Requirements

for the Degree of

MASTER OF SCIENCE

THE UNIVERSITY OF TEXAS AT ARLINGTON

MAY 2017

ACKNOWLEDGEMENTS

I would like to thank Dr.Brian Dennis for making me a part of the CFD Lab, and for his constant guidance and motivation during the course of my thesis work. I also thank Siddarth Chinatamani for his invaluable help, guidance, and mentor-ship. I would like to thank Dr.Bo P Wang and Dr.Zhen Xue Han for being a part of my thesis defense committee and for their valuable insights and inputs on my work.

I am grateful for all the wonderful people I have met over the past three years in grad school. I thank my friends at the CFD lab, my friends at UTA, and my roommate, for their encouragement, and moral support.

Finally, I would like to express my gratitude to my family for their unwavering support of my goals, and thank them for the love and care they have shown all my life.

MAY 3rd, 2017

ABSTRACT

NUMERICAL ANALYSIS OF A FLAPPING ELLIPTIC FLAT PLATE IN HOVER: A STUDY OF THE LEADING EDGE VORTEX DYNAMICS.

C. VIVEK NAIR, M.Sc.

The University of Texas at Arlington, 2017

Supervising Professor: Brian Dennis

Flapping flight is an area of research that is gaining a lot of prominence in engineering, especially with the increase in interest in applying the flapping mechanism of natural fliers to small scale MAVs. The ongoing contributions to this field include studies finding optimal wing shape, flap frequency, and flap trajectories. Flapping flight is an unsteady aerodynamic mechanism, and consists of 3 interactive forces: delayed stall, rotational circulation, and wake capture. The dominant lift generating mechanism is the leading edge vortex (LEV). Natural fliers optimize their flap to gain maximize LEV stability. For our research we simulate 2 cases of Reynolds number (225 and 500) and find the max circulation of the LEV as a function of an experimental parameter called formation number (FN). For flapping flight FN is defined as the ratio between the stroke length and chord projection. We also conduct a vortcity transport analysis to understand the various flux budgets that contribute to the vorticity during the flap cycle.

TABLE OF CONTENTS

LIST OF ILLUSTRATIONS

# 1. Introduction

Every bird, animal, and insect that is capable of flight does so by flapping its wings. Tiny insects fly through a complex maze of trees and shrubs while birds fly large distances with minimal energy use. Certain animals have evolved flapping flight to navigate and travel across large distances quicker; countless millenia of evolution acting as the perfect optimization tool. It can therefore be stated that flapping flight is very well suited for low Reynolds number aerodynamics. While the physics of steady, fixed-wing flight is well studied, researchers have only just begun to delve into the physics of flapping flight. While early work on flapping wings have been done to understand animal flight [1], the immense interest in bio-inspired engineering and bio-inspired micro aerial vehicles (MAVs) means a more in-depth inquiry is required for the efficient design and control of such vehicles.

Flapping flight is characterized by unsteady, low Reynolds number(Re) aerodynamics. Typical Reynolds numbers range from 100 to $10^5$. Due to the unsteady nature of flapping flight the existing mechanics of steady flight do not accurately capture the force generation in such fliers. Infact it was the application of steady flight physics to the explain the flight of the bumblebee that led early scientist to incorrectly conclude that a bee should not be able to fly. While consequent research has better captured the mechanics of flapping flight and indeed shown that a bee does generate enough lift force to fly. This unfortunate myth is still used as an example of scientific deficiency. The difficulties in capturing flapping physics is compounded by the inherent miniature size of such fliers.

Natural fliers generate the required forces by flapping their wings at relatively high frequencies ranging from 10 $Hz$ to 200 $Hz$. See table 1 for some properties of insects.

| Name of insect | $M$ Mass (mg.) | $S$ Total wing area (mm.²) | $S_b$ Body cross-section (mm.²) | $R$ Length of longer wing (mm.) | $\nu$ Frequency of beating (sec.$^{-1}$) | $V$ Velocity of flight (m./sec.) | $a$ Ratio time of lowering to raising |
|---|---|---|---|---|---|---|---|
| DIPTERA: | | | | | | | |
| *Tabinus bovinus* | 276 | 184 | 63 | 15·5 | 96 | 4 | 1·5 |
| *Sarcophaga carnaria* L. | 45 | 36 | 12 | 7·0 | 160 | 2 | 1·5 |
| *Musca domestica* | 12 | 20 | 4·5 | 5·5 | 190 | 2 | 1·7 |
| *Volucella pellucens* Meig. | 73 | 78 | 39 | 12 | 120 | 3·5 | 1·2 |
| HYMENOPTERA: | | | | | | | |
| *Xylocope violacea* | 614 | 172 | 47 | 18 | 130 | 4 | 1·3 |
| *Bombus terrestris* Fabr. | 388 | 142 | 74 | 16 | 130 | 3 | 1·1 |
| *Vespa germanica* | 187 | 98 | 29 | 14 | 110 | 2·5 | 1·3 |
| *Vespa crabro* L. | 567 | 260 | 100 | 22·5 | 100 | 6 | 1·8 |
| *Apis mellifica* L. | 78 | 42 | 27 | 8·5 | 250 | 2·5 | 1·3 |
| *Amonophila sabulosa* V. del | 45 | 42 | 82 | 9·0 | 120 | 1·5 | 1·2 |
| LEPIDOPTERA: | | | | | | | |
| *Papilio podalirius* | 300 | 3600 | 52 | 37 | 10 | 3·5 | — |
| *Vanessa atalanta* L. | 134 | 1080 | 31 | 27 | 10 | 4 | — |
| *Pieris brassica* L. | 127 | 1840 | 35 | 31 | 12 | 2·5 | — |
| *Macroglossa stellatorum* L. | 345 | 400 | 68 | 20 | 85 | 5 | 1·3 |
| *Plusia gamma* L. | 144 | 440 | 36 | 18 | 48 | 1·5 | 1·1 |
| COLEOPTERA: | | mem. m.+ely. | | | | | |
| *Melontha vulgaris* Fabr. | 961 | 402 642 | 100 | 28 | 46 | 2·5 | 1·5 |
| *Cetonia aurata* | 537 | 260 370 | 68 | 20 | 86 | 3 | 1·3 |
| *Lucanus corvus* | 2600 | 800 1220 | 250 | 36 | 33 | 1·5 | 1·0 |
| *Telephorus fuscus* | 109 | 116 166 | 20 | 12·5 | 72 | 0·8 | 1·4 |
| NEUROPTERA: | | | | anterior | | | |
| *Brachytron pratense* Mull. | 557 | 1200 | 36 | 36·5 | 33 | 5 | 1·4 |
| *Calopteryx splendens* Harr. | 120 | 850 | 13 | 30 | 16 | 1·5 | 1·6 |
| *Pyrosoma minium* Harr. | 38 | 355 | 8 | 25 | 27 | 0·6 | 1·2 |
| *Panorpa communis* L. | 30 | 176 | 8 | 14·5 | 28 | 0·5 | 1·6 |
| *Orthetrum caerulescens* Fabr. | 248 | 1080 | 22 | 32·5 | 20 | 4 | — |
| *Aeschna mixtra* Latr. | 530 | 1380 | 30 | 39·5 | 38 | 7 | 1·7 |

Figure 1: insect performence data [1]

By flapping their wings at high frequencies, insects exploit and utilize high lift mechanisms such as leading edge vortices (LEV), wake capture, and rotational lift. Figure 2 describes the Clap and fling Mechanism. These mechanisms combined create a phenomenon called dynamic stall. Dynamics stall is seen in aerodynamic bodies subjected to pitching or oscillations, where the trajectory and high angle of attack of the wing generate the LEVs that enhance lift but are unstable in nature. The lift force measured during dynamic stall shows a spike in lift followed by loss of lift. However, natural fliers adapt their wing frequencies and flapping trajectory to maximize lift over time.

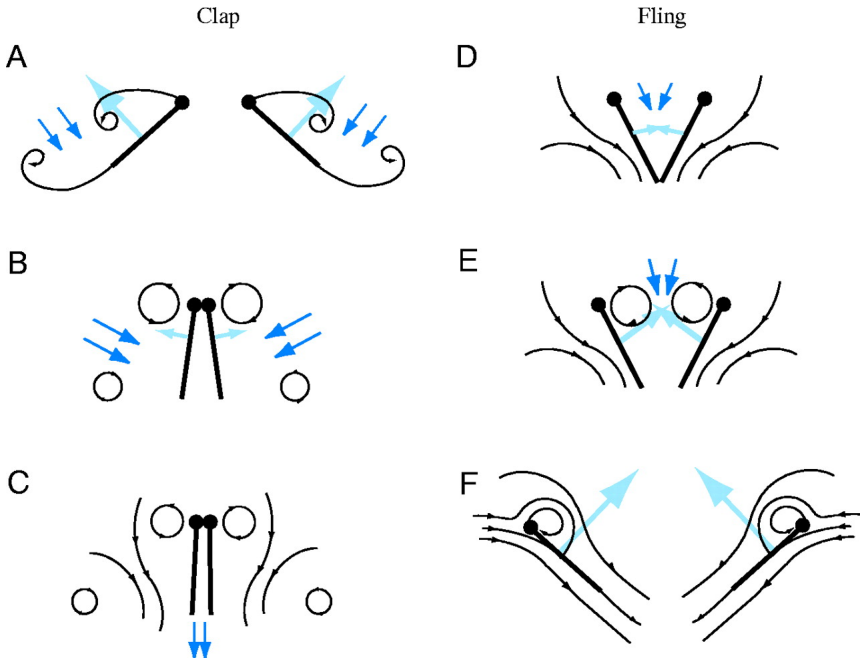


Figure 2: Schematic of the clap and fling Wing Mechanism [2].

The dominant lift generating mechanism and the motivation of this study is the leading edge vortex (LEV). An LEV, as the name suggests, is a vortex on the leading edge of the flapping wing. As the angle of attack of the wing increase, the airflow over

the wing separates over the leading edge but reattaches before it reaches the trailing edge. In such cases, a leading edge vortex occupies the separation zone above the wing. In this case, because the wing translates at a high angle of attack, a greater downward momentum is imparted to the fluid, resulting in substantial enhancement of lift[2]. The generation of the LEV is dependent on a number of variables such as the frequency of flap, angle of attack of attack , stroke amplitude and geometry of wing. Figure 3 shows the velocity vectors in an LEV captured around a HummingBird wing [3]. The LEV structure can be identified at the leading edge by the circular nature of the velocity vectors.

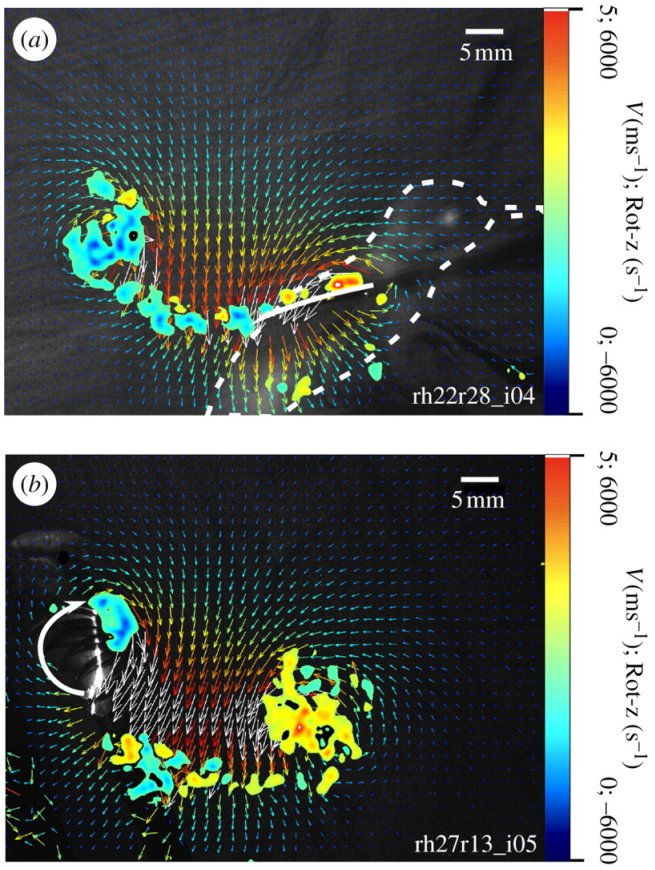


Figure 3: DPIV image of the contours of the velocity vectors around a Humming Bird wing. [3].

The advantages of flapping flight lie in their flight efficiency, and relative simplicity in design [9]. As such research and studies finding optimal wing shape, flap frequency, and flap angle of attack and their comparison can be seen as significant contributions to this field. Of interest to this study is a parameter called Formation number(FN) along with the mechanisms for vorticity transport in the LEV [5],[6],[10]. Formation number is a non-dimensional parameter that defines the maximum circulation that a vortex can attain during its formation. It is based on the Kelvin-Benjamin variational principle for axisymmetric vortex rings. Formation number in the case of flapping wings is defined numerically as the ratio between stroke length and chord projection[11]. Formation number is important to flapping flight as it shows LEV growth and stability, allowing researchers to look for optimum flap frequencies and trajectories. While experimental studies of LEV structures have been performed[12], it is not possible to capture LEVs in different planes and make accurate analysis in 3 dimensions. Using CFD we are able to explore in detail the various mechanisms and their effects on LEV growth and stability.

## 2. Literature Review

Early work on physics of Flapping wings started around the 1950's with M.F Osborne's research quantifying the wing kinematics in insects [1]. Osbornes work is one of the earliest attempts at quantifying all the kinematic forces acting on a flapping wing (see figure 4). Most, if not all,of the fundamental research on flapping wings were carried out by experimental biologists[13]. Weis-Fough worked on the aerodynamics of insects and hummingbirds in hover [14]. He conducted experiments to analysis

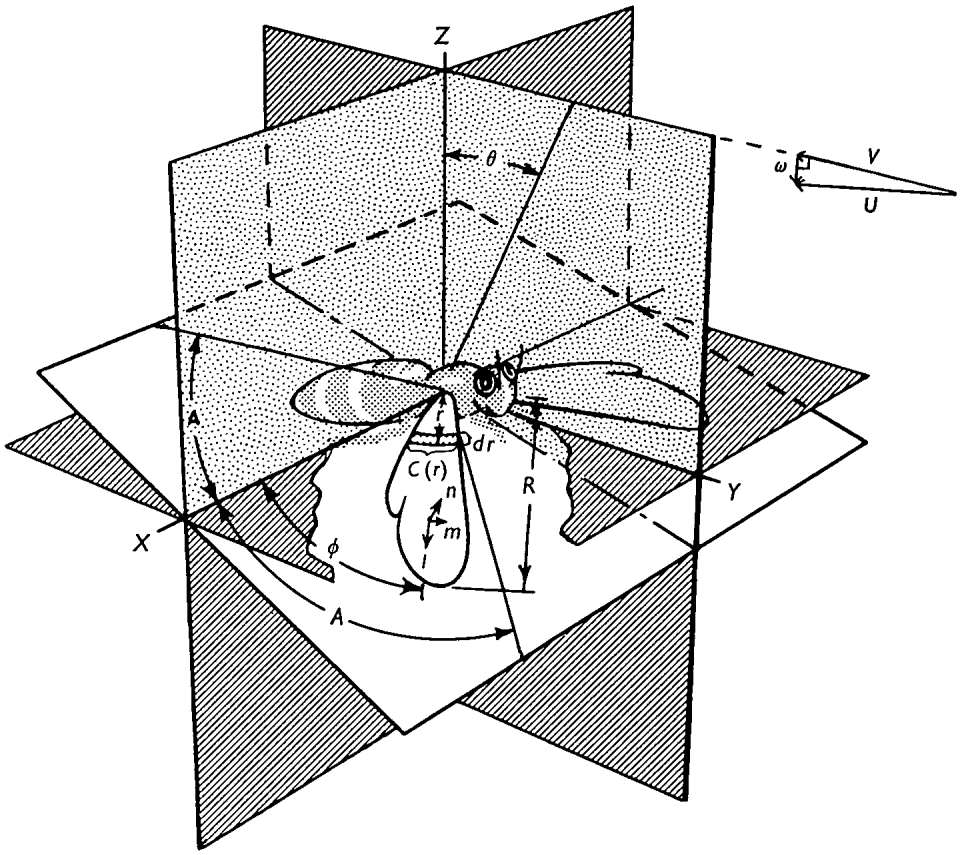


Figure 4: Schematic of Osbornes insect model [1]

the lift coefficients and cross verify his results with quasi steady analytic models and inferred that hovering is performed on the basis of well established steady-state flows. He is credited with explaining the clap and fling mechanism of flight seen in many insects. Ellingtons research, a six paper series, reviews Weis-Foghs assumption that flapping flight can be predicted by quasi-steady models, and a conclusion opposite to Weis-Foghs is reached (refer [13] for subsequent papers authored). Ellington revisits the quasi-steady model in his first paper and while some accurate analytic results were obtained, the final inference was that a more robust understanding of insect flight is required. Ellingtons second and third paper presented a variety of kinematic and morphological experimental data. This data is useful in validating future models. Ellingtons remaining papers offer a comprehensive and new model on wing kinematics, aerodynamics and power requirements seen in natural fliers. Ellingtons papers are the first series of papers to capture each flight mechanism separately and describe its effects on force generation. An analysis of the different kinds of fling mechanisms were also studied [15]. Vandenberg et al. used a scaled up robotic Hawkmoth wing that accurately mimicked the real flier in flight [16]. It was inferred that the circulation growth and lEV structure clearly showed that dynamic stall was the dominant unsteady mechanism for high lift production. Sane et al. revisit the theory of wing aerodynamics and kinematics [2]. They utilize a robotic fly wing to test analytic models and notice a large discrepancy n force prediction. They conclude that the force measurements depend on 3 distinct yet interactive measurements: delayed stall, rotational circulation and wake capture. Fry used 3D infrared high speed cameras to capture continuous wing and body kinematics of free-flying fruit fly, during hover and forward flight [17]. The experiment was 'replayed' using a dynamically scaled robot wing and forces measured. It was found that time averaged models overestimated flight costs, while instantaneous measurements and analytic model predictions had

too many discrepancies. This points to a more significant role played by unsteady forces.

Lentink and Dickinson experimented to identify the individual forces that stabilize the LEV [4]. They stipulated that the major forces in play are the coriolis and centrifugal force, and that angular force imparted dude to back and forth motion did not significantly contribute to overall LEV stability. They also suggest that LEV stability is independent of Reynolds number.Figure 5 shows the LEV structure and stability due to a rotating motion at a specified angle of attack.

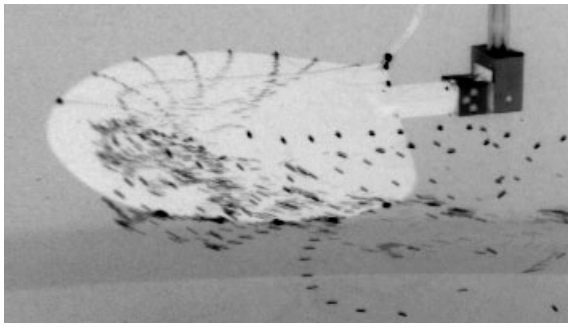

Figure 5: LEV structure and interaction shown using hydrogen bubbles. [4]

Polema et al. measured the time dependent three-dimensional velocity field around a flapping wing for the first time, using a dynamically scaled wing in mineral oil [18]. Typical results for two cases, an impulsive start and a simplified flapping pattern, are reported. It was seen that the LEV structure consisted of pair of stable counter-rotating vortices. Wang et al. compared a CFD model, experimental and quasi-steady forces in a generic wing undergoing sinusoidal motion [19]. Comparisons were made between 3D experiments and 2D computations. It was inferred that 2D models under-predicted vortex shedding with respect to 3D observations. Also the lift and drag measurements agreed favorably in most cases. For larger animals, Mujires

used DPIV(digital particle image velocimetry) to show that nectar feeding bat is able to increase lift by 40 percent using attached LEVs during slow forward flight [20]. They showed that unsteady aerodynamics mechanisms is also used by larger animals. Warrick et al. analyzed the LEV structure on a hummingbird in hover [3]. It was seen that the LEV structure enhanced lift production during the entire wing half-stroke. However, the 2D DPIV capture of the LEV showed characteristics different from those observed in smaller insects like the Hawkmoth. Gharib used a piston-jet setup to show that the maximum circulation a vortex ring can achieve during its formation occurs at a non-dimensional number called Formation number [5]. The Formation number was given a numerical definition and its universality was tested under different parameters. Gharib explained that the presence of Formation number can be attributed to the kelvin-Benjamin variational principle for axisymmetric vortices. Figure 6 shows vortex generation at different FN starting at 4 ,12 and 30.

Dabiri showed that vortex ring pinch off can be delayed for an impulse jet in counter flow if the energy of LEV is decreased during formation and/or the energy delivered by vortex generator is increased [6]. He inferred that this delay occurs as the kelvin-benjamin principle must be met. Krueger showed the effects on formation for a jet in co-flow [10]. As expected the Formation number was reached earlier than in no flow condition, a result the opposite of that seen in counter flow. This results may hold key insights into the low FN of flapping wings as it can be seen as being in a kind of co-flow condition. Figure 7 is illustrative of the counter flow condition where FN is higher than normal. O'Farrel experimented on formation and pinch-off of non-axisymmetric vortex rings [21]. He observed that maximum circulation of vortex can be determined using equivalent diameter of jet nozzle. Additionally the time of vortex ring pinch off is found to be constant along nozzle contours, and independent of relative variations in the local curvature. Milano defined a Formation number

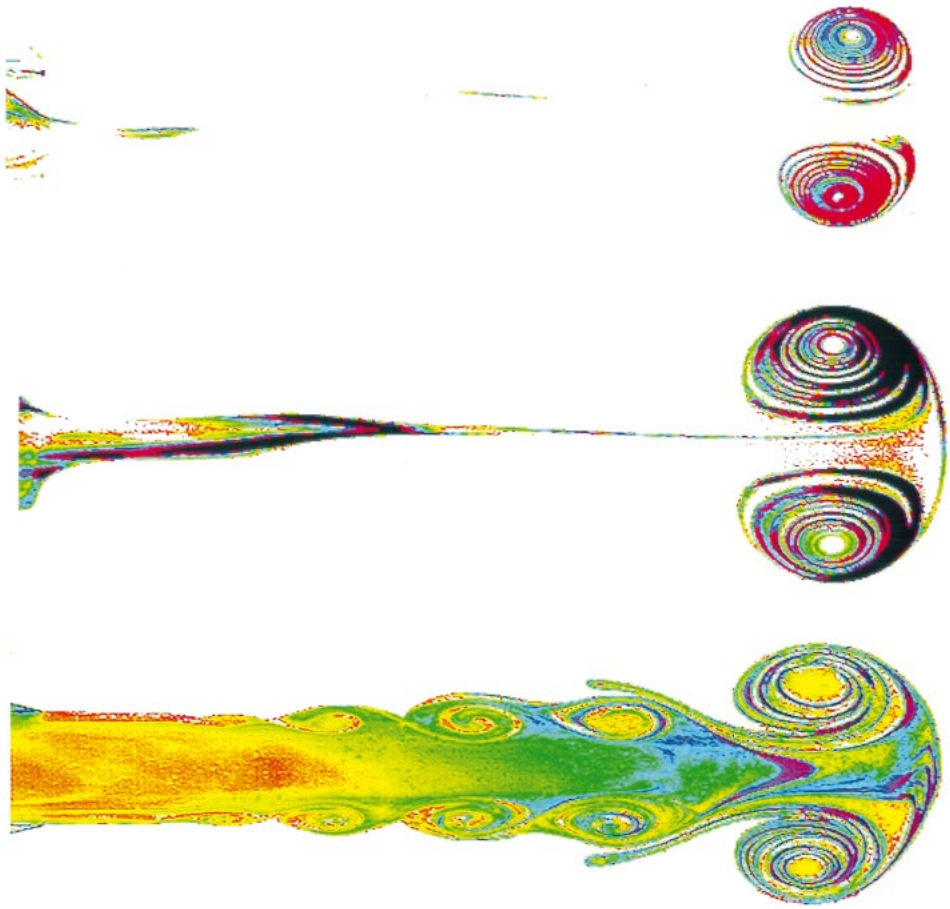

Figure 6: Vortex generation for various Formation numbers at 4, 12, 30 respectively [5].

equation for flapping flat plates [11]. It is defined as the time integral of velocity of leading edge over the chord projection taken in the direction of half stroke. Ringuette experimentally investigated the force generated by the unsteady vortex formation of low-aspect-ratio normal flat plates with one end free [22]. It was seen that the tip vortex produces a significant maximum in the plate force,and suppressing its formation results in a force minimum. Kim studied the vortex structures of translating low aspect ratio flat plates [23]. It is seen that the vortex formation is significantly different for rigid, flexible and curved rigid thin plates of the same aspect ratio. The literature discusses and compares the results of formation number and hydrodynamic

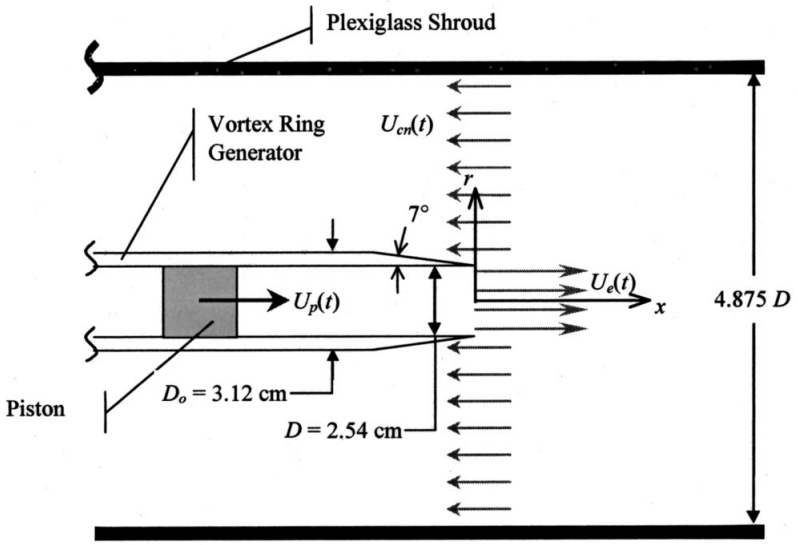


Figure 7: Schematic of the vortex generator in counter flow experiment by Dabiri [6].

forces observed.Pannah et al. analyzed the vorticity transport within the LEV generated on a rectangular flat plate of aspect ratio 4 [7]. Analysis was done on the inboard 25 percent and 50 percent of the flat plate. It is seen that although spanwise velocity is significant, spanwise convection of vorticty is insufficient to balance the flux of vorticity from the leading edge layer. Pannah carried out further experimental analysis of a plunging flat plate to analyze the vorticity transport [7] (see figure 8). The experiment showed the presence of a secondary vorticity, of opposite sign to the primary vortex, act as a sink to the LEV. They carried out a planar vorticity transport analysis and the literature discusses the results of the analysis.

Finally, at the CFD lab here at UT Arlington, Chintamani et al. carried out numerical analysis of flat plate in hover to study wake capture in 3D [8]. He analyzed the vorticity transport and formation number. It was seen that the formation number matched previous experimental analysis done with flapping plates. It was also seen that the flux budgets in the vorticity transport equation were largely symmetric in nature along each instance of the flapping cycle (see figure 9). The current study

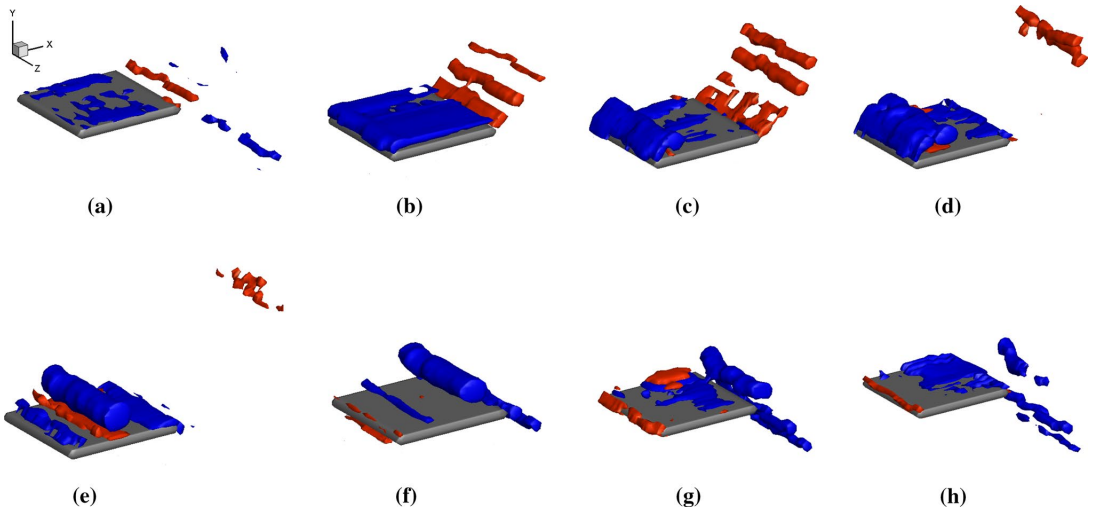


Figure 8: Vortex formation on a plunging plate at Re 10000. [7]

utilizes Milano's formulation of formation number [11], Wangs trajectory formulation [19] , and for the vorticity transport, the curl of incompressible Navier-Stokes equation leads to a formulation as shown in Buchholz[7]. The present study uses numerical analysis in the form of CFD simulations to study the effect of wing geometry, under varying parameters of flap frequency, on the formation number and vorticity transport of the LEV structure. The numerical formulation is discussed in chapter 5 followed by results and discussion in chapter 6.

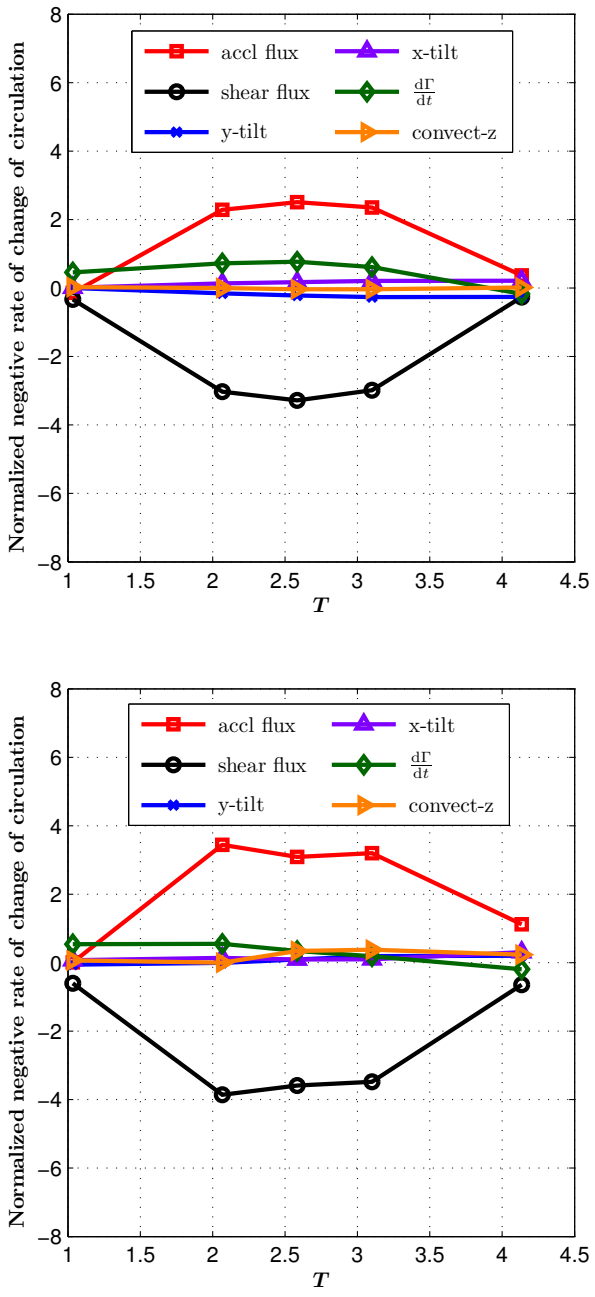


Figure 9: Vorticity transport analyzed at 25 and 75 percent plane on a rectangular flat plate.[8]

## 3. Motivation, Goals, and Milestones

The motivation to conduct a study of the LEV dynamics of an elliptic flat plate in hover is to better understand the flap mechanism of natural fliers. The elliptic geometry is chosen for its simplicity of design and is modeled to a size similar to the wings seen in the *Bombini* tribe of bees. The effects of geometry and flap frequency on circulation is studied, with two cases being tested, one within the range of frequency observed in such natural fliers, and one outside of it. Tests are also done to analyze the robustness of Formation Number(FN) and the vorticity transport carried out at different planes. The study is done at Reynolds number ($Re$) 225(within the range of natural fliers), 500(outside the range of natural fliers) and is a function of flap frequency $f$. The vorticity transport is analyzed to study the contributions of the individual flux budgets. The work on low Reynolds Number aerodynamics has helped in gaining a stronger understanding of the incompressible Navier-stokes equations and how to carry out CFD analysis. This work has given me the opportunity to work with CFD software ANSYS fluent® and mesh generation software Pointwise®. The work has enhanced my coding skills in MATLAB and C programming and also introduced me to glyph, and scheme scripting. This work has also given me the chance to dive deeper into bio-inspired Engineering and helped improve my knowledge on the research and work being carried out by others in the field . Part of this work has been accepted to the ASME-IMECE 2017 conference. We hope to carry out further simulations and publish the findings in a journal.

# 4. Methodology

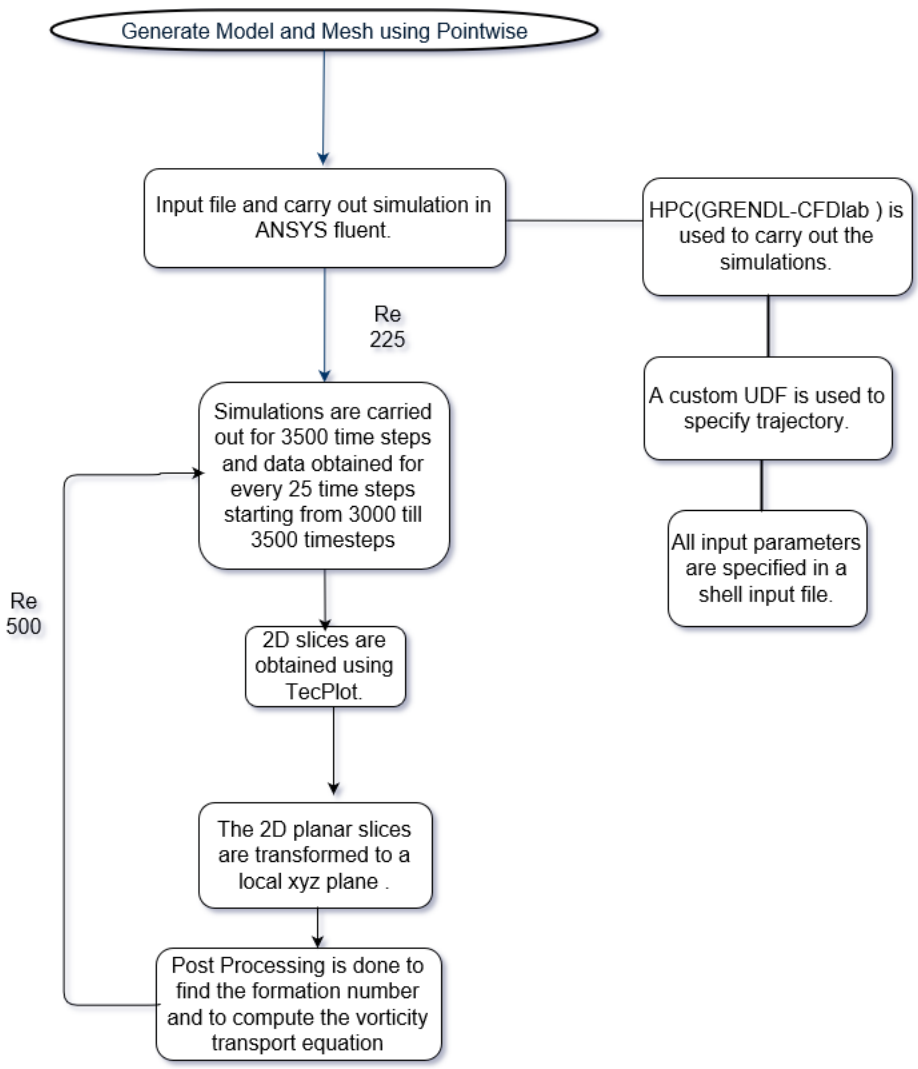


An elliptic flat plate model is created and the mesh generated around it using a commercial grid generation software Pointwise®. The Grid geometry and Topology are explained in section 4.1. The boundary conditions are specified and the mesh file exported to ANSYS fluent®. We use ANSYS fluent® to run the simulation. The

flow solver is described in section 4.2. A case file is created and the simulations run on a high performance computer (HPC), GRENDL-CFDLab. A custom UDF is used to specify the trajectory and the input parameters are specified in a separate input file. The trajectory is explained in section 4.3. The simulation runs for 3500 time steps, creating data files at every 25 timestep interval starting from 3000 to 3500 time steps. For the post-processing, the data files are converted to .plt files to be used in Tecplot®. In Tecplot® we cut slices at 0, 25, 50 and 75 percent of quarter perimeter. The values of the perimeter location for each timestep is found using a custom MATLAB® code(see section 4.6). A point and normal function is used to specify the planar slice. A total of 84 slices are obtained. The slices are transformed using custom MATLAB® code (see section 4.7). This is done to make FN and vorticity transport computations in the Lagrangian reference frame.(see section 4.8 and 4.9) The simulation is carried out at $Re$ 225 and $Re$ 500.

4.1 Model Geometry and Grid Topology

An elliptic flat plate with root chord length $1.2mm$ is modeled (see figure 10). The aspect ratio is kept as 3. The plate has a thickness of 0.05 mm. The upstream, downstream, top, and bottom boundaries are kept at a length of 40 chord lengths from the plate. The root side of the boundary is modeled as a symmetry plane and the other side is placed at 5 chord lengths in the spanwise direction.

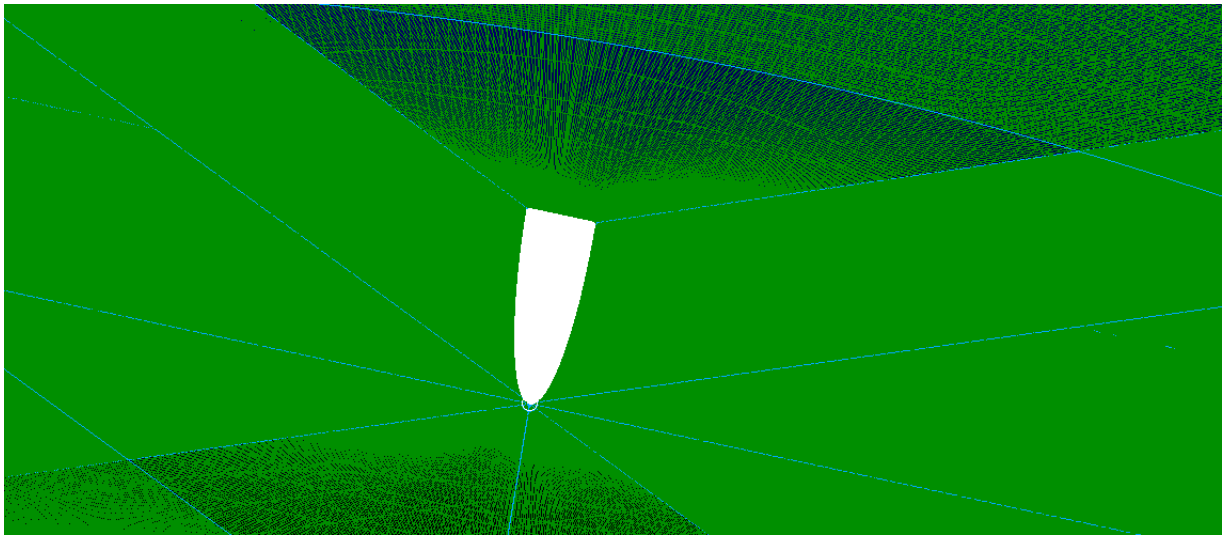

Figure 10: Geometry and domain around the flat plate.

A structured grid Mesh is generated using commercial software Pointwise® (see figure 11). The grid is meshed to 3 million cells to keep congruence with the earlier work [8], nevertheless a grid refinement study is done at 1.5 million, 3 million and 6 million. The domain is divided into 2 regions: (i) an inner circular domain region of radius 25 chord lengths. Around the flat plate the mesh is kept fine and expands radially outwards(ii) an outer domain region consisting of an inner-square domain and outer-square domain. The trajectory UDF acts on the inner domain and the

inner square of the outer domain. The outer domain joins the inner domain and the boundaries.

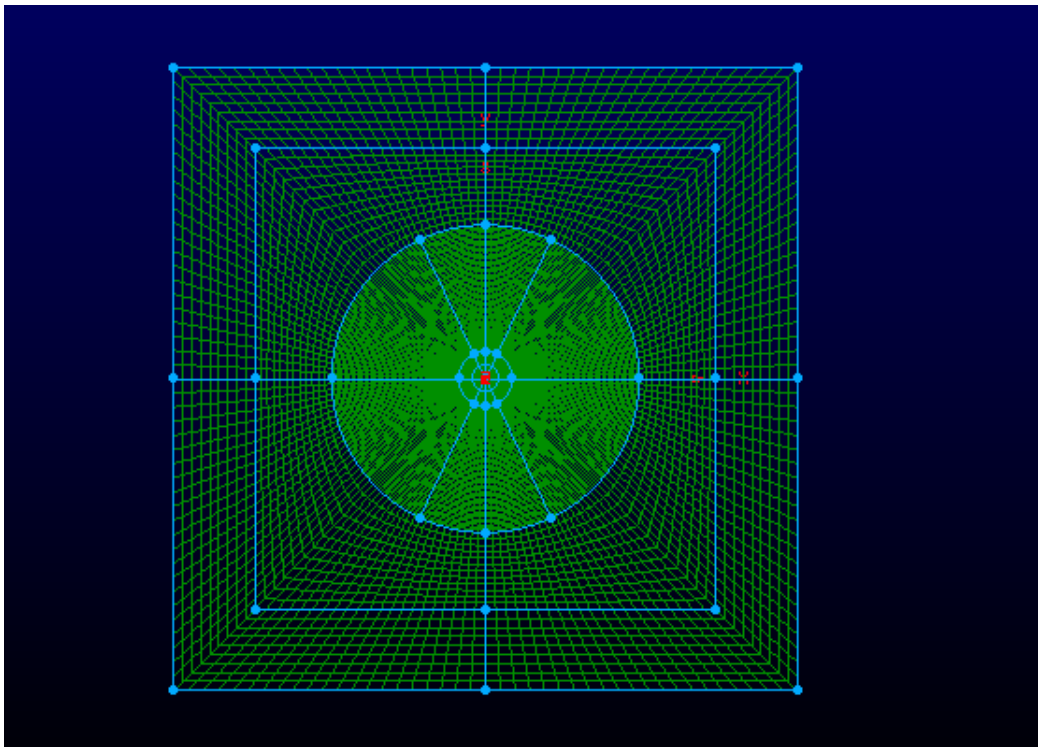

Figure 11: Domain viewed along the span(z-axis normal to plane). The circular inner domain rotates and translates to the match the flapping trajectory. The outer Domain consists of the inner square and outer square segments.

The dynamic mesh function in ANSYS fluent® is used to simulate the flapping cycle. The movement of the grid nodes was defined using user defined functions (UDF). The nodes on the inner domain translate and rotate to the flapping trajectory of the elliptic plate( described in section 4.3) The UDF for the motion of the outer domain is such that the nodes at the boundary are stationary and the nodes at the interface translate with the same translation velocity of the inner domain. Figure 12 shows the motion of the wing.

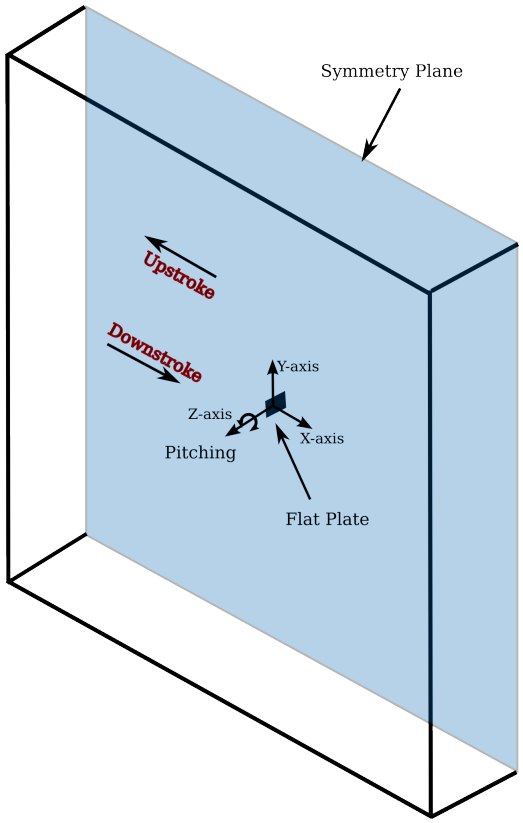


Figure 12: a parametric view of the domain showing direction of flap and pitch axis.

4.1.1 Boundary Conditions

- A symmetry boundary condition is applied at the symmetry plane.
- The plate surface is considered as a no slip wall.
- Dirichlet boundary conditions with 0 gauge pressure is enforced on all other boundaries.
- The interface between the inner domain and outer domain is modeled as a sliding interface.
- The solution is initialized for a velocity of $10^{-6}$ in the x-direction.

### 4.1.2 Grid Independence Study

A grid independence study is done at 1.5, 3, and 6 million cells and the lift force coefficients are measured for the 4th upstroke( see figure 13). Although there is a minor force peak difference between the 3 million and 6 million cells, due to qualitative similarities and computational constraints the 3 million cell is used for simulations.

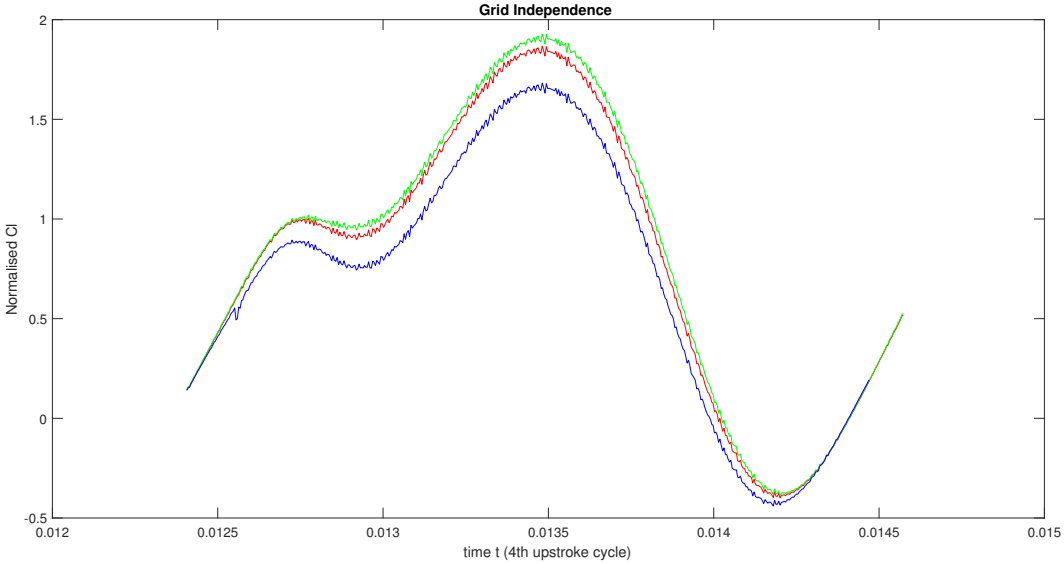


Figure 13: Normalized $C_L$ vs time $t$. Blue line shows 6 million, red line shows 3 million, and green line shows 1.5 million.

## 4.2 Flow Solver

The 3-dimensional incompressible Navier-Stokes equations(N-S) were solved using ANSYS fluent®. The solver uses the finite volume formulation to solve the N-S equations. The governing equations are given by

$$\nabla . u = 0 \tag{1}$$

$$\frac{\partial u}{\partial t} + u.\nabla u = -\frac{1}{\rho}\nabla P + \nu.\nabla^2 u \tag{2}$$

$u$: velocity vector

$\rho$: density,

$P$: pressure field

$\nu$: kinematic viscosity.

An implicit pressure based approach is used to solve to solve the equations. The pressure-velocity coupling is done using a coupled scheme which solves the momentum and pressure based continuity equation together. The momentum equation is discretized using a third order MUSCL scheme; MUSCL stands for Monotonic Upstream-Centered Scheme for Conservation Laws. The continuity equation is discretized using a second order differencing scheme. Time marching is done using a second order formulation. The under relaxation is kept at the 0.5 and the flapping cycle discretized to 1000 equal time steps.

The entire run consists of 3500 time steps or 3 and a half flap cycles with each run taking around 3 and a half days. The fourth cycle is considered for post-processing as the results are stable and cyclic. The solver was run on GRENDL (HPC) at the CFD-Lab using 4-6 nodes depending on availability.

### 4.2.1 A Brief Summary of MUSCL Scheme

As mentioned earlier MUSCL stands for Monotonic Upstream-Centered Scheme for Conservation Laws. It is a high order scheme that uses a finite volume method and provides a highly accurate numerical solutions for a given system, even in cases where the solutions exhibit shocks, discontinuities, or large gradients. Developed by Bram

Van Leer it is an extension of the finite volume scheme developed by Godunov [24], [25]. MUSCL based numerical schemes extend the idea of using a linear piecewise approximation developed in the Gudonov scheme to each cell by using slope limited left and right extrapolated states.

4.3 Flapping Tajectory

We follow the flapping trajectory described in Wang et al.[19] and shown in figure 14. The wing follows a sinusoidal flapping and Pitching motion with the translation occurring in the horizontal plane and the pitching occurring about the spanwise axis.

$$x(t) = \frac{A_0}{2} cos(2\pi f t) \tag{3}$$

$$\alpha(t) = \alpha_0 + \beta sin(2\pi f t + \phi) \tag{4}$$

.

Where $x(t)$ is the position of wing center,

$\alpha(t)$ is the wing orientation with respect to the x-axis.

The angular, and translation velocities are obtained by differentiating the above equations to yield

$$U_0(t) = \frac{dx(t)}{dt} \tag{5}$$

$$\Omega(t) = \frac{d\alpha(t)}{dt} \tag{6}$$

$A_0$ is the stroke amplitude,

$\alpha_0$ is the initial angle of attack,

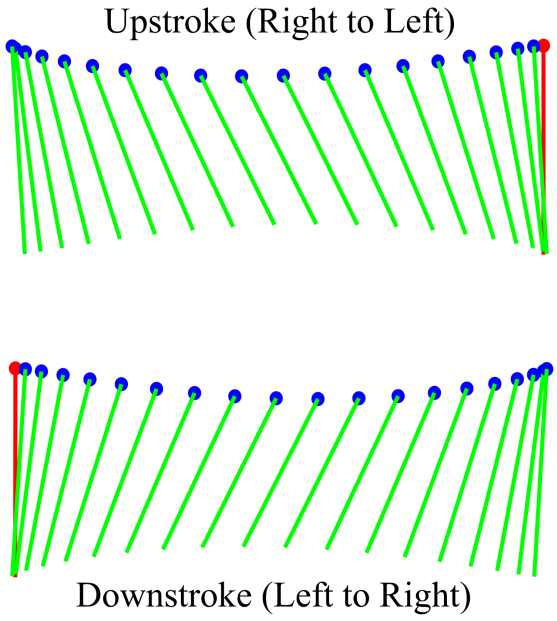


Figure 14: Flapping trajectory $\phi = 0$ (symmetric rotation). Red line shows start of each flap. Circle denotes the leading edge.

$\beta$ is the amplitude of pitching angle of attack,

$f$ is the flapping frequency, $\phi$ the phase difference between $x(t)$ and $\alpha(t)$.

The Reynolds number is based on maximum wing velocity $Umax$ and chord length $c$, and is defined as

$$Re = Umax(c/\nu) = \pi f A_0(c/\nu) \tag{7}$$

For the 2 cases of $Re$ 225 and 500

The phase difference $\phi = 0$

$(A_0/c) = 3$,

$\alpha_0 = \pi/2$,

$\beta = \pi/4$.

The frequency $f$ is changed to get the desired $Re$ for the two cases.

A single flap cycle is considered complete when the wing is back to its original position at 0 time(i.e one complete upstroke and downstroke).

4.4 Frequency Formulation

The numerical analysis is done for $Re$ 225 and 500.

From Equation (7) :

$$f = \frac{Re}{\pi A_0 (c/\nu)} \tag{8}$$

We keep the flapping amplitude $A_0$ constant. Changing the frequency to match the $Re$ desired. The flapping frequency for $Re$ 500 is calculated to be : $5.41974 * 10^2\ Hz$
The flapping frequency for $Re$ 225 is calculated to be : $2.41890 * 10^2\ Hz$.
To find the value of individual time step for simulation we find the reciprocal and divide by 1000 ( the number of timesteps for each cycle ).

$$t = \frac{1}{(f \cdot 1000)} \tag{9}$$

This gives us :

The time step size for $Re$ 500 as $1.84511 * 10^-6\ s$.

The time step size for $Re$ 225 as $4.13411 * 10^-6\ s$.

## 4.5 Post Processing

### 4.5.1 Ellipse Perimeter and Slice Locations

The formation number and vorticity transport are calculated at planes normal to the $0, 25, 50, 75$ percent quarter perimeter locations (see figure 15). The total perimeter is calculated using the equation

$$perimeter = \pi \cdot [3(a+b) - \sqrt{((3a)+b) \cdot (a+(3b))}] \tag{10}$$

Where $a$ and $b$ are the semi major axis and semi minor axis respectively.

Since we are only finding the locations at the leading edge we find the quarter perimeter value $Qp = (Perimeter/4)$.

The coordinates at 0, 25, 50, 75 percent quarter perimeter for the 3000th time step are calculated using a MATLAB code to ensure accuracy to the $4th$ decimal. We use the same code to find the coordinates $+0.1$ and $-0.1$ percent on either side of

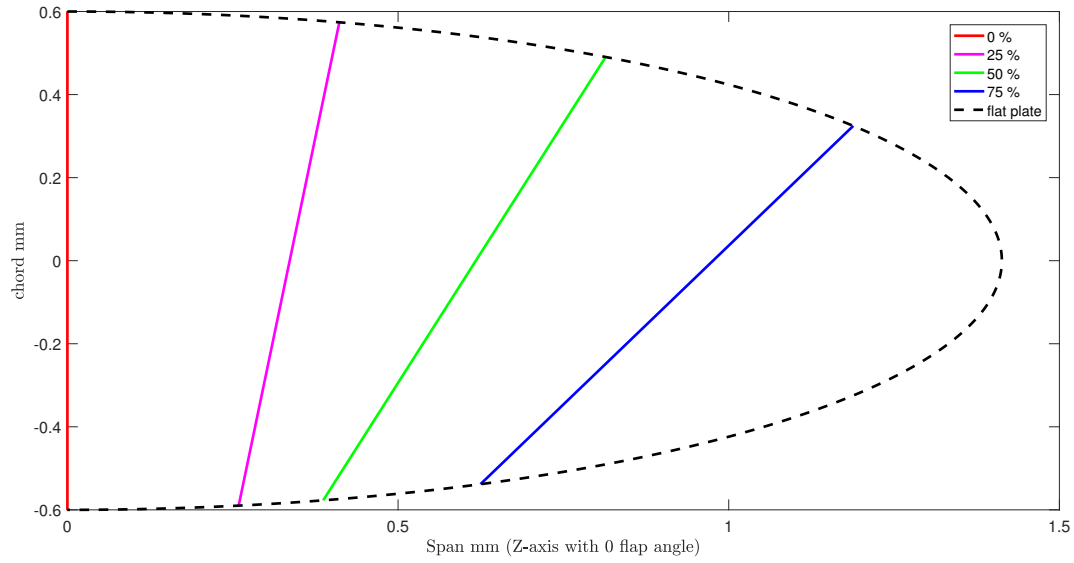


Figure 15: Location of plane at 0, 25, 50 , 75 percent quarter perimeter.

these points to used later to find normals and track the points as they move through the flap cycle.

The coordinates are as follows:

for 0 percent perimeter: $(z, y)$=$(0, 0.0006)$

for 25 percent perimeter: $(z, y)$=$(0.0004112, 0.0005740)$

for 50 percent perimeter: $(z, y)$=$(0.0008138, 0.0004904)$

for 75 percent perimeter: $(z, y)$=$(0.00118833, 0.0003246)$

The coordinates of these points as the flat plate moves through the flap cycle are calculated using a custom MATLAB code(See Appendix A).

4.5.2 Transformation Matrix

Numerical analysis ,for all $Re's$, was done on 2D slices taken normal to the surface in the direction of flap for the last 500 time steps representing one half flap cycle. We transform the individual slices to a local coordinate system that moves with the LEV, thus representing a Lagrangian reference frame. We use a custom MATLAB code to achieve this.

$$TransformationMatrix(t) = \begin{bmatrix} nxx(t) & nyx(t) & nzx(t) \\ nxy(t) & nyy(t) & nzy(t) \\ nxz(t) & nyz(t) & nzz(t) \end{bmatrix} \tag{11}$$

The transformation matrix converts each slice from a global $x$,$y$,$z$ plane to a local $x'$,$y'$,$z'$ plane with unit normal $[0, 0, 1]$. The transformation matrix is a function

of time. We know the columns of the transformation matrix are the images of the basis vectors. If we find an orthonormal basis that includes unit normal $n$ the rows of the rotation matrix we seek will be these basis vectors.

Keeping this in mind The transformation matrix is constructed as follows:

- Since we wish to transform to the $z'$ axis, the last row consists of basis vectors from the unit normal $n$. In our case we use the tangent to the curve at the selected points.
- The second row consists of basis vectors for a normal taken taken orthogonal to unit normal $n$. In our case it is the line normal to the selected points.
- The first row consists consists of the final basis vectors obtained by taking the cross product of the basis vectors.
- For MATLAB code refer Appendix B.

The transformation Matrix is used to transform the axes, velocity, and vorticity magnitudes(which can be considered as scalar values), and their differentials(which constitute a coordinate transformation of a second order Tensor ).

The scalar transformation is given as:

$$\begin{pmatrix} xvel'(t) \\ yvel'(t) \\ zvel'(t) \end{pmatrix} = \begin{bmatrix} nxx(t) & nyx(t) & nzx(t) \\ nxy(t) & nyy(t) & nzy(t) \\ nxz(t) & nyz(t) & nzz(t) \end{bmatrix} \cdot \begin{pmatrix} xvel(t) \\ yvel(t) \\ zvel(t) \end{pmatrix} \tag{12}$$

And the tensor transformation is as follows:

$$[Q'] = [T^T][Q][T] \tag{13}$$

Where $[Q]$ is the matrix of original variables (in our case the differentials of vorticity w.r.t to space).

$[T^T]$ is the transpose of the transformation matrix.

$[T]$ is the transformation matrix.

4.5.3 Formation Number (FN)

The Formation number is defined as the ratio of distance traveled by the wing to the total area projected [11]. Its a non-dimensional quantity that signifies maximum circulation an axisymmetric vortex can attain. In the case of flapping flight this signifies the maximum circulaton an LEV can attain before detaching. The Formation number is explained by the Kelvin-Benjamin variational principle. While early research [5] stipulated the FN to be around 4, It is shown in our research that the number is not as stable as expected, and varies with variation in frequency and shape. The present work focuses on frequency changes affecting $Re$ and its effect on FN.

$$T(t) = \int_{t_0}^{t} \frac{U_0(t) + \frac{1}{2}c\Omega(t)cos(\theta(t))}{csin(\theta(t))}dt \tag{14}$$

Where $T$ is the formation number, $U_0(t)$ the translational velocity at a given instant(In our case a non-dimensionalized velocity), $c$ the chord length, and $\Omega(t)$ the angular velocity.

4.5.3 Vorticity Transport Equation

A flux budget analysis is done to quantify the source and sink terms that contribute to the growth of LEV. The vorticity transport is obtained from the rate of change of circulation about a closed curve :

$$\frac{\mathrm{d}\Gamma}{\mathrm{d}t} = \frac{d}{dt}\oint_{\partial A} u \cdot \mathrm{d}s \tag{15}$$

Substituting the Navier-Stokes equation to the RHS of equation(9) yields:

$$\frac{\mathrm{d}\Gamma}{\mathrm{d}t} = \int_A [\nabla \times (\omega \times u)] \cdot n_A dA - \oint_{\partial A} \frac{dp}{\rho} - \oint_{\partial A} a_I \cdot \mathrm{d}s + \oint_{\partial A} \nu \nabla^2 u \cdot \mathrm{d}s \tag{16}$$

Expanding upon the first and second integrals on right hand side of equation(10) gives us

$$\frac{\mathrm{d}\Gamma}{\mathrm{d}t} = -\int_A u_z \frac{\partial \omega_z}{\partial z} \mathrm{d}A + \int_A \left( \omega_x \frac{\partial u_z}{\partial x} + \omega_y \frac{\partial u_z}{\partial y} \right) \mathrm{d}A - \oint_{\partial A} (u \cdot n_{\partial A}) \, \omega_z \mathrm{d}s - \oint_{\partial A} a_I \cdot \mathrm{d}s + \oint_{\partial A} \nu \nabla^2 u \cdot \mathrm{d}s \tag{17}$$

The equation for vorticity transport is verified with Panah et al.[7] The first term on the right hand side of equation(9) represents spanwise convection of the leading edge vorticity. The second term represents the vorticity generated due to tilting (in this case local x and y tilting). The third term represents shear layer flux. $a_I$ is the local acceleration in the inertial reference frame. The final term represents diffusion of vorticity through boundaries.

The acceleration term vanishes for a purely translating flap, however, in our case there exists both a translation and pitching motion. This acceleration term which also includes centrifugal and Coriolis forces is calculated by adding all known values and treating the acceleration as the only unknown. The diffusion terms are too small and are therefore neglected.

## 5. Results and Discussion

The flap cycle run for *Re* 225 shows LEV formation and circulation for a majority of the upstroke with the LEV detaching at 80 percent of upstroke. Figure 16 shows the LEV captured at time step 3250 across the 4 planes. The blue and red show regions of opposing spanwise vorticty $\omega_z$. The $\omega_z$ is captured in the global plane before transformation. The regions of vorticity in blue attached to the leading edge of the plate represents the LEV. It is interesting to note a region of opposing vorticity connected just below the LEV . This is in agreement with the observations made by Panah et al.[7]that the LEV region contains a vortex sheet of opposing voritcity that acts as a sink.

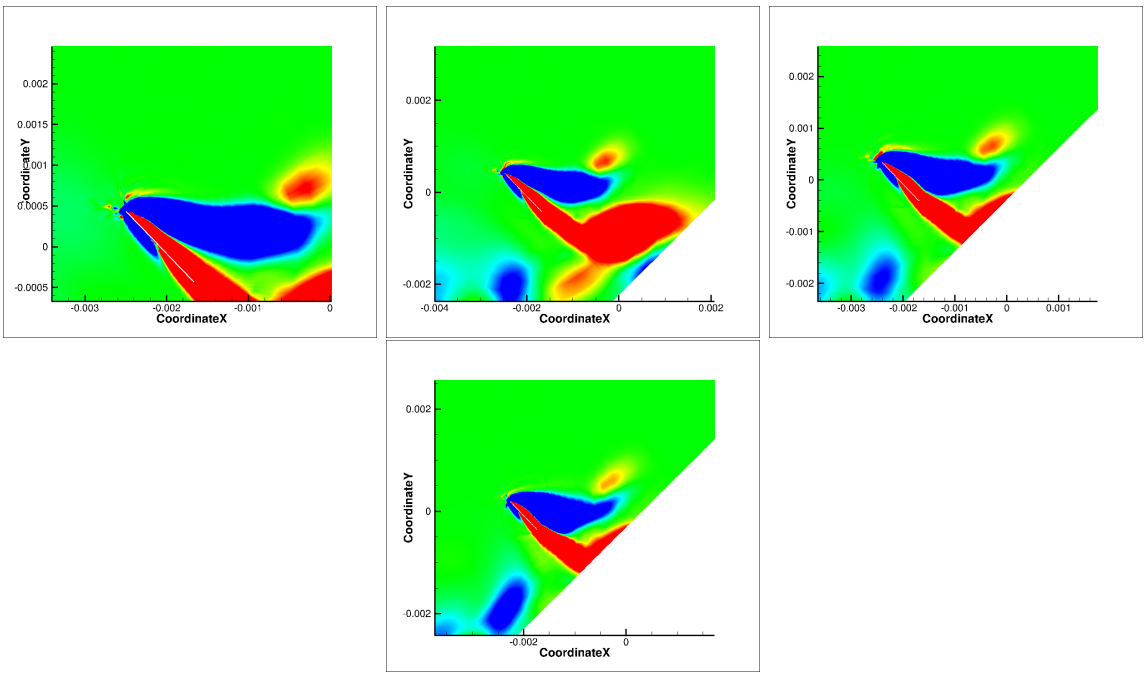


Figure 16: clockwise from top left: 2-D slice at 0, 25, 50, 75 percent plane for case 1, *Re* 225 at time step 3250.

At $Re$ 500 the LEV formation and detachment occurs almost immediately with a new LEV formation starting around 25 percent upstroke. The second LEV goes on to detach around 80 percent upstroke. Figure 17 shows the LEV captured at time step 3100 across the 4 planes. Here large opposing vorticities around the LEV structure are clearly visible and possibly play an important role in LEV detachment so early in the upstroke. It must be noted that this is not seen during LEV reformation further into the upstroke. The entire Upstroke at 0 percent plane for $Re$ 225 and $Re$ 500is shown in **Appendix A**.

At each of the 4 planar regions, we obtain 21 planar slices, which captures the LEV growth and detachment through the $4th$ upstroke cycle. The planar slices are transformed into a Lagrangian reference frame following the LEV as it forms through

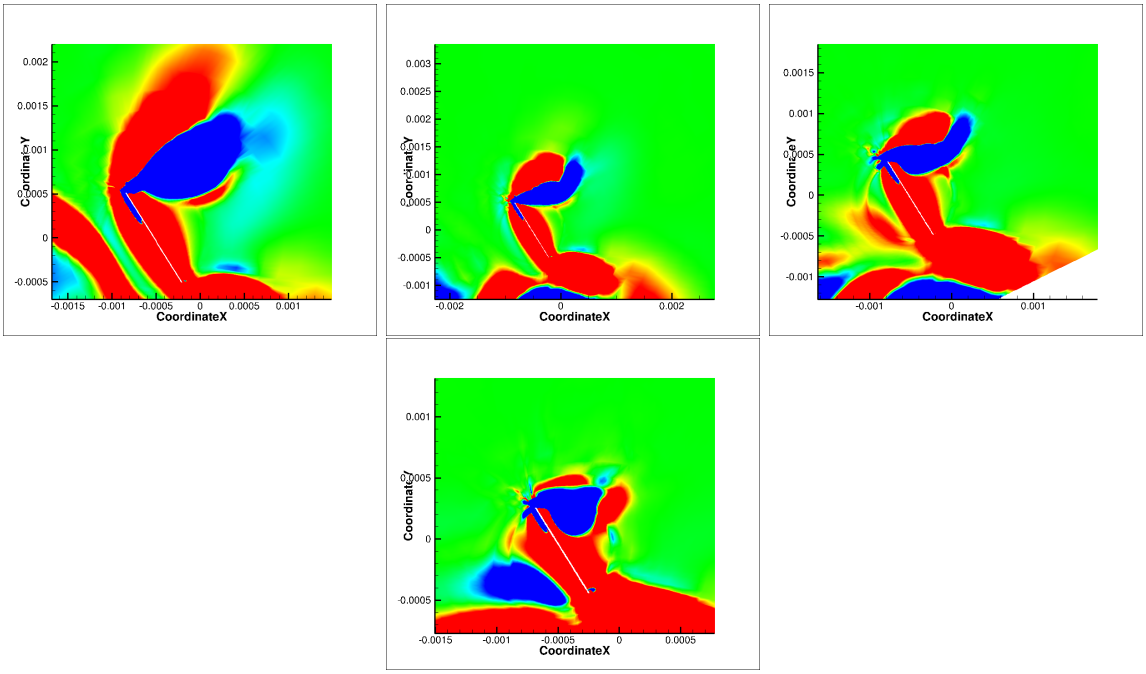


Figure 17: clockwise from top left: 2-D slice at 0, 25, 50, 75 percent plane for case 1, $Re$ 500 at time step 3100.

the upstroke. The Formation number analysis and vorticity transport are done on the transformed planes.

## 5.1 Circulation vs Formation Number Analysis

At *Re* 225 the formation number for a flapping elliptic plate is around 2.6 (see figure 18). We see the circulation increases as we go from root to tip. This is in line with the results seen by Poelma et al. [18]. This shows that for a flapping wing the formation number is much less than its standard definition given by Milano and Gharib [11] i.e the non dimensional formation number for maximum circulation in axisymmetric vortex is 4. It is interesting to note that the circulation at the 75 percent plane is lower than other planar regions till half way through the formation of the LEV. This indicates a strong dependence on wing geometry to the LEV growth across the planes. The entire vortex sheet irrespective of the circulation at individual planes breaks off at the FN 2.6.

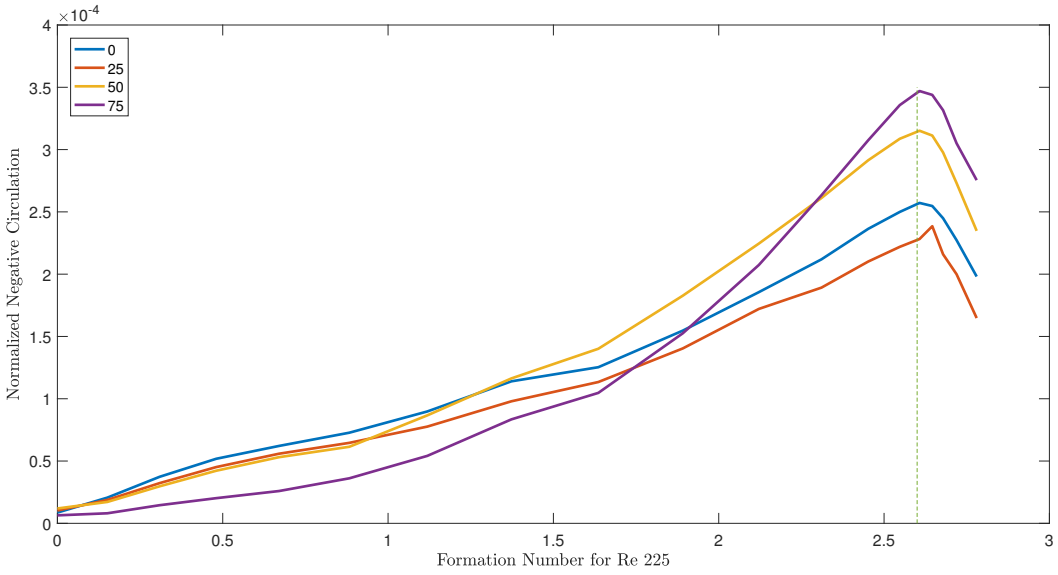


Figure 18: Normalized circulation vs Formation number at 225

The analysis at *Re* 500 yields a much more chaotic graph (see figure 19). However, there are a few key insights to be seen here. The graph can be studied as 2 regions. Region 1 is from the FN 0 to FN 1. Region 2 from FN 1 till end of flap. It is seen that the LEV detaches quite quickly at FN 0.7 in region 1. However, the circulation at 75 plane does not increase as fast as other planes. In region 2 the new LEV is formed and breaks off at around the location of FN 2.6 with circulation along each plane following almost the same pattern as seen in *Re*225. Here the max circulation is much lower than seen in *Re*225. While not completely understood, it is hypothesized that the LEV detaches around FN 0.7 without reaching the maximum circulation seen further into the upstroke due to the large opposing vorticity around the LEV being far to destructive and destabilizing instead of acting as just a sink.

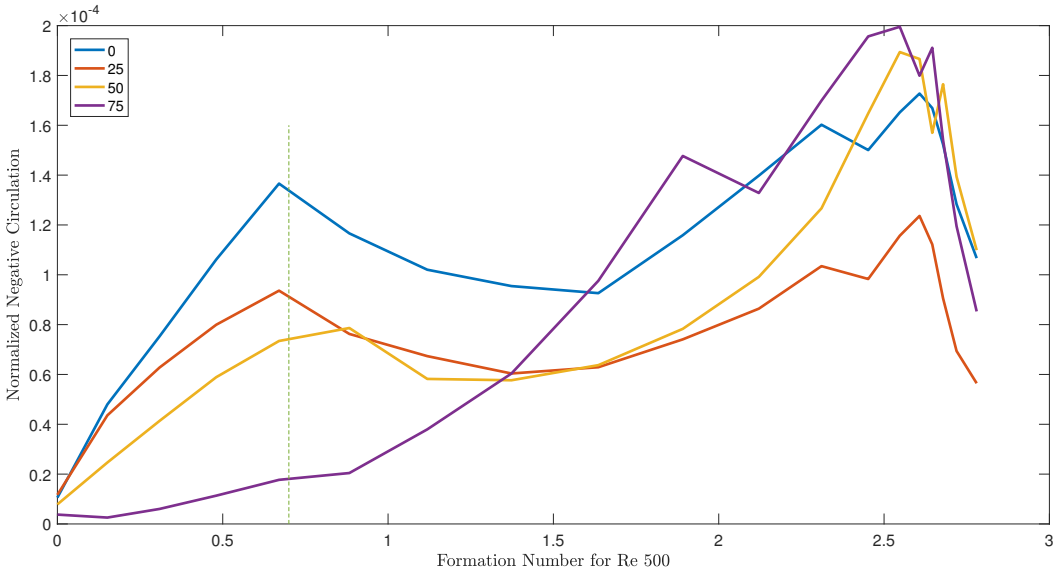


Figure 19: Normalized circulation Vs Formation number at 500.

Inferences

The aim of this study was to test the robustness of the FN number definition as an indicator of LEV stability. Theoretically the FN should be the same irrespective of the $Re$ as both the projected area and the projected distance remain the same. As the FN is itself an experimental parameter the definition might be dependent on other parameters. It must be stated that for instances of multiple LEV shedding, as seen in $Re500$, it is only appropriate to take the first LEV shedding as the FN of the cycle to define LEV stability. It is interesting to see in both cases atleast one instance of LEV detachment happens around a similar FN value (i.e 2.6). Although in the case of $Re500$ the FN value at the second instance of shedding holds less significance, physically it implies that an LEV detachment occurs around the same point in the upstroke for both $Re's$. Unfortunately, no concrete correlations can be made without further simulations. Our present study suggests that the $Re$ is indeed a contributor to LEV stability. It must be kept in mind that for the present study the $Re$ was a function of frequency and not amplitude of flap and further simulations are required to see if this dependence holds for all parameters. At the moment of LEV detachment the circulation values differ at each plane, with the 75 percent plane having the most circulation. We can intuitively say that LEV stability depends on the stability of the entire vortex sheet and individual planar circulation values help in pointing to the region where the detachment is initiated. The elliptical flat plate dimension is comparable to that of a bumble bees wing. Bee wings usually flap around $Re$ 190 to 245. From our analysis it can been seen that the vortex detaches almost at 80 percent of upstroke for $Re$ 225. Essentially the LEV is attached for a major part flap cycle. While a translating flap cannot accurately capture all the forces in a rotating-reciprocating trajectory, the trends suggest that natural fliers have evolved to maximize their LEV stability. The circulation at 75 percent for both the cases

show a similar trend (see figure 20). This suggests that the circulation mechanisms at the tip are dependent on factors that have not been captured in this study. It is hypothesized that the mechanism feeding the circulation is highly 3-dimensional and a dependent on the span wise location of the plane with the LEV detachment being initiated closer to the root. Finally the low FN values suggests that the flapping wing physics can be hypothesized as a vortex formation in co-flow.

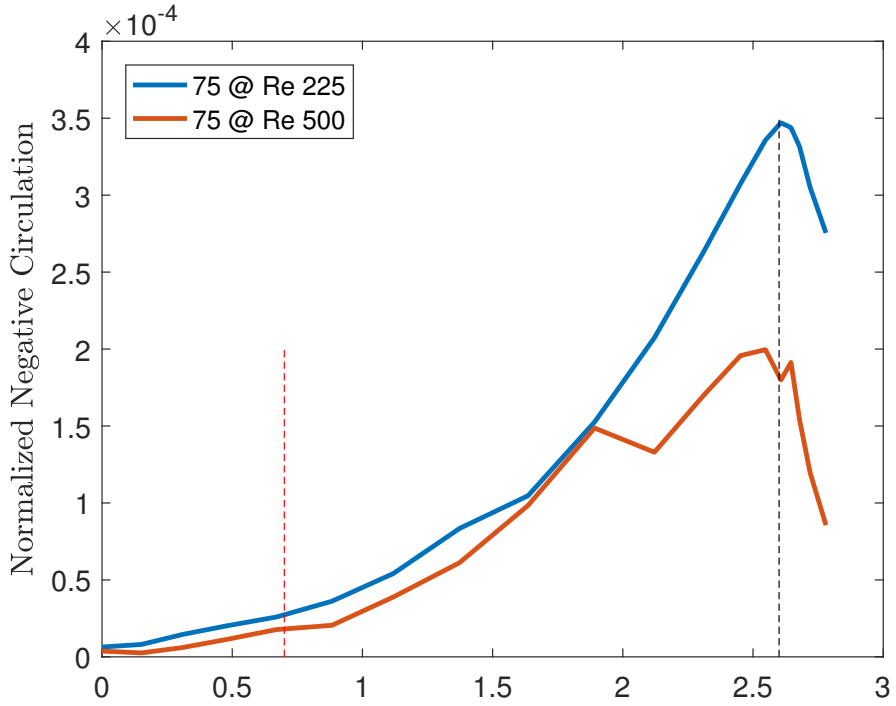


Figure 20: Circulation vs Formation number for 75 percent plane for both cases of $Re$.

5.2 Comparison Elliptical Flat Plate to Rectangular Flat Plate at *Re* 225

We compare the results obtained to the previous work done on rectangular flat plates[8]. The flat plate simulation was carried out on identical trajectory ,flap frequency, flap amplitude and consequently same *Re*. The rectangular flat pate has a aspect ratio of 3.

The circulation vs formation number plot for rectangular and elliptic flat plates are shown in figure 20 and 21 respectively. It is observed here that for the given *Re*, the value of FN is the same for both the cases indicating that the overall LEV stability is not that dependent on geometry. However, in the case of the rectangular flat plate the circulation follows a decreasing trend across the planes, while the opposite is seen for elliptical flat plates. Infact, in the case of the rectangular flat plate the circulation at 75 percent plane has the lowest circulation for the entire cycle. Therefore the geometry can be said to affect individual trends in planar circulation. The magnitude of circulation for the ellipse is much higher in comparison to the rectangular flat plate. It is hypothesized that this disparity is seen due to the use of aspect ratio

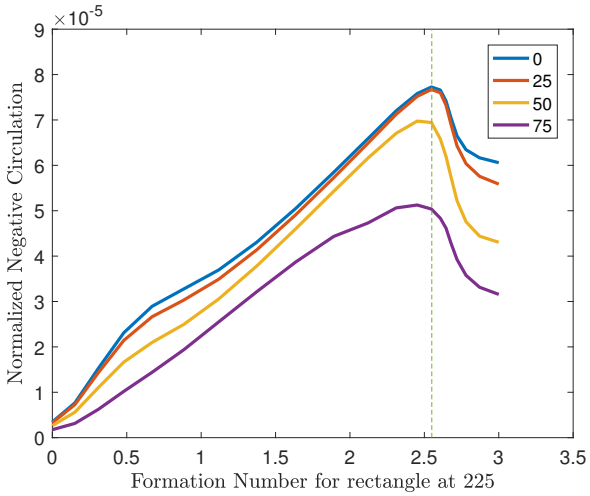


Figure 21: Circulation vs formation number for a rectangular flat plate in hover at *Re* 225

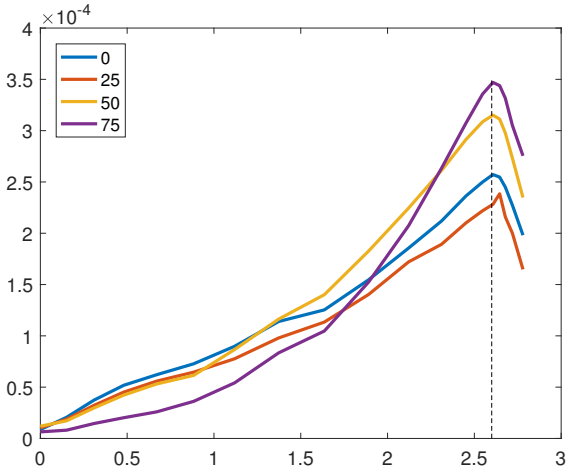


Figure 22: Circulation vs formation number for a elliptic flat plate in hover at *Re* 225

as the variable for geometry comparison. It is our suggestion that the aspect ratio (AR) is not an accurate parameter for comparison. Although the AR is the same, the root to span distance is different for the rectangle and wing, and therefore, might not yield an accurate comparison between geometries especially the planar slices. A more accurate comparison can be made by keeping the span constant and changing the mean chord length.

## 5.3 Vorticity Transport Analysis

For **case 1 at Re 225**, the flux budget for the symmetry plane is just as expected with the dominant shear flux and acceleration flux acting as source and sink terms respectively, and the tilting, stretching, and spanwise convection terms being negligible. It is also seen that the fluxes drop off at FN 2.5. Figure 21 shows the flux budgets at symmetry plane.

Evaluating the vorticity transport at 50 percent, we see that as we move away from the symmetry plane the contribution on the tilting terms and span wise convection increases quite drastically (see figure 21). The over all contributions of each of

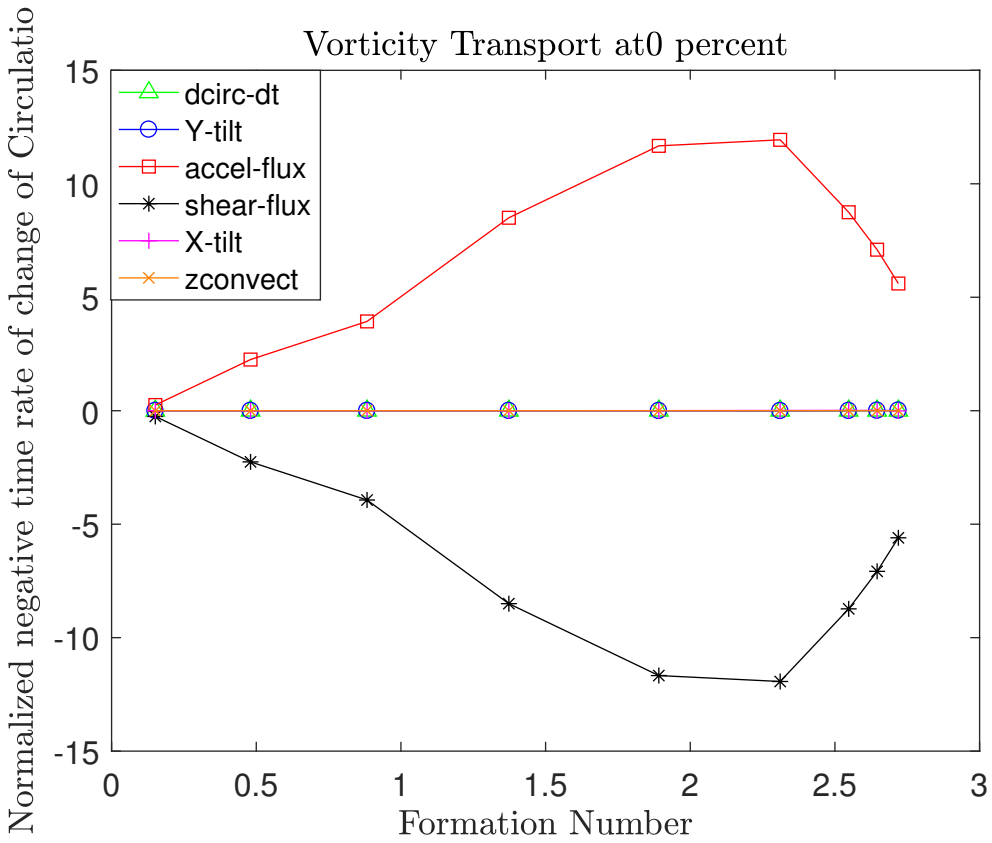


Figure 23: Normalized fluxes vs Formation number on a transformed plane at 0 percent of quarter perimeter *Re* 225.

the fluxes is also a lot higher especially around FN 2.5 indicating that as the circulation increases there is greater out of plane transfer of energy. The dominant terms are still Shear flux and acceleration flux. The x-tilting term acting as a sink is quite interesting to note as we do not see a significant y-tilting term in what is supposed to be a set of flux budgets that usually cancel each other out.

The flux budgets in the 75 percent plane shows the highest magnitudes around FN 2.5 (see figure 22). This correlation is expected as the plane also has a higher circulation near the 1.7 to 2.5 FN region. The out of plane fluxes predictably have higher contributions. Even so, it is interesting to note that the spanwise convection term is much more pronounced in this plane. It should be noted that the x-tilting

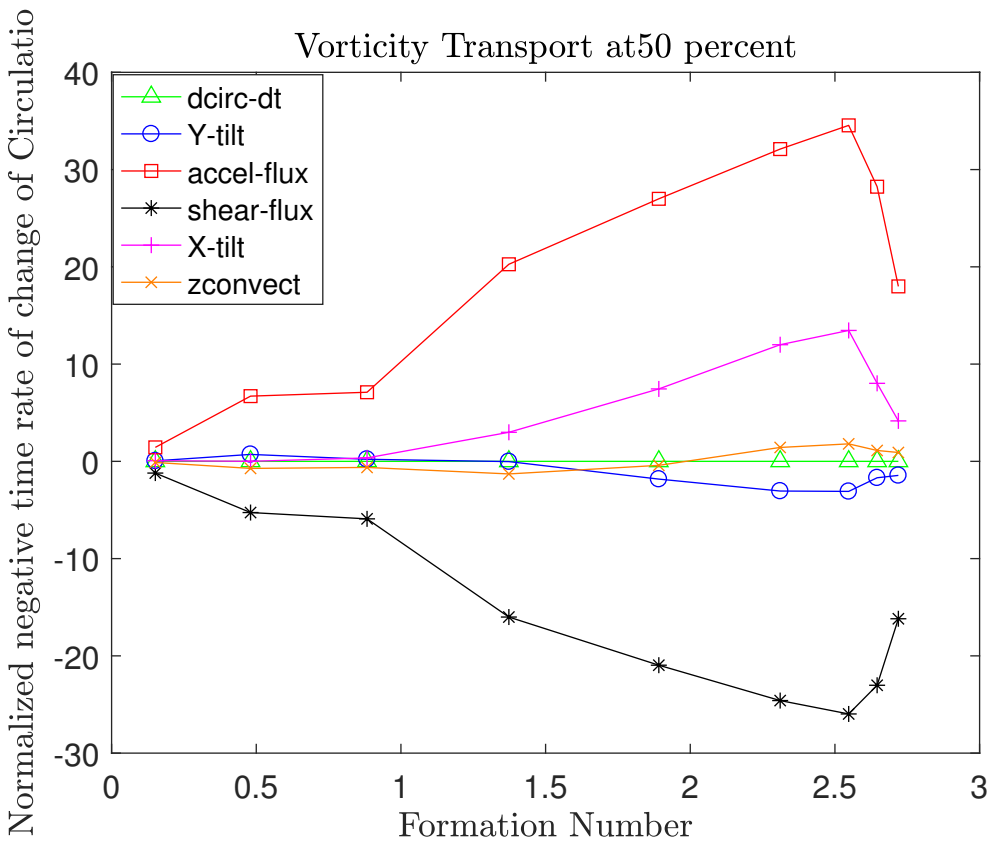


Figure 24: Normalized fluxes vs Formation number on a transformed plane at 50 percent of quarter perimeter for *Re* 225.

term and the z-convection term at 75 percent show trends similar to the x-tilting and z-convection terms at 50 percent, albeit a lot stronger, reinforcing the observation that the circulation across individual planes is affected by geometry, and is generally dependent on the curvature.

The flux budgets as we move from 0 percent span to 75 percent show certain peculiarities. The dominant source and sink terms are the shear flux and acceleration flux respectively. This reinforces the inferences made from the rectangular flapping wing simulations by Chintamani et al. [8] that the role of wing kinematics is to act as a drain for the vorticity generated as a result of boundary layer roll up and maintain an LEV.

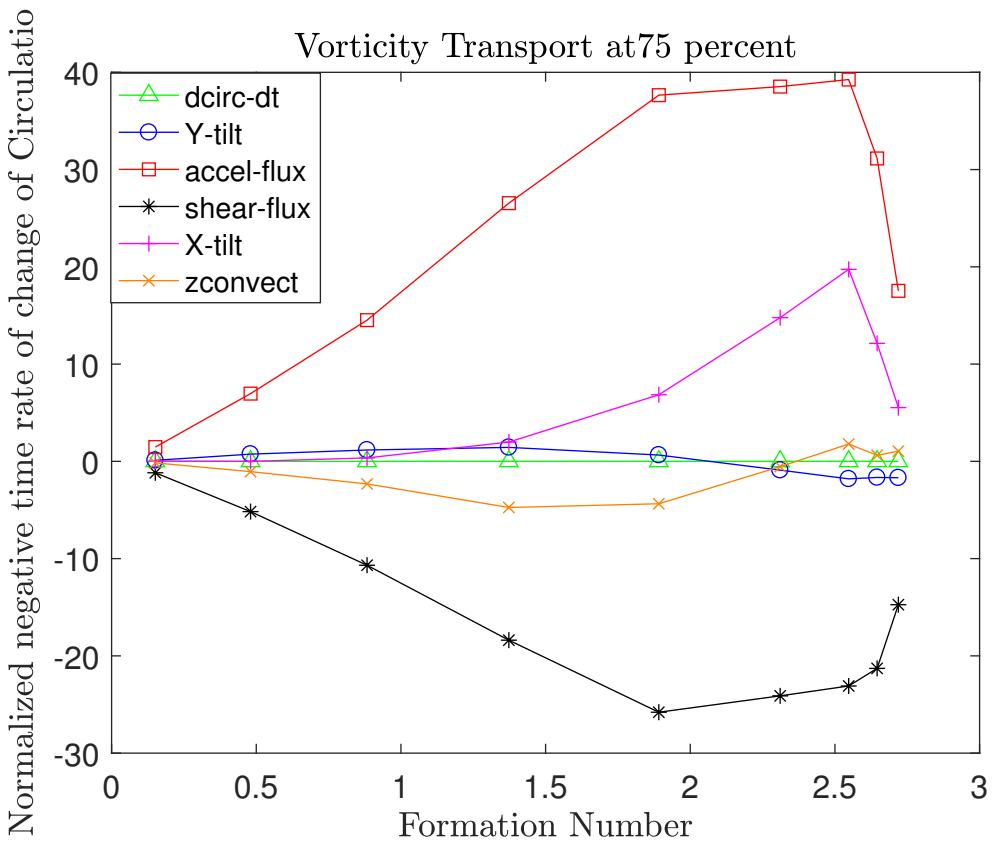


Figure 25: Normalized fluxes vs Formation number on a transformed plane at 75 percent of quarter perimeter for *Re* 225.

However, it is also seen that the tilting terms(especially the Y-tilting) become more pronounced and are unsymmetrical and as a result are non zero, as we move towards the tips of the wing (see figure 25). The convection along z axis while remaining minimal shows an increase in contribution to the over all vorticity transport as we move further away from the root of the wing span. This clearly shows the 3-dimensional nature of the LEV. While it was seen in the rectangular flat plate simulations [8] that the the LEV was highly 3 Dimensional at the tips, in the case of the elliptical flat plate this 3-dimensionalilty is seen through out the wingspan. It can be inferred from this that leading edge geometry clearly affects vorticity transport.

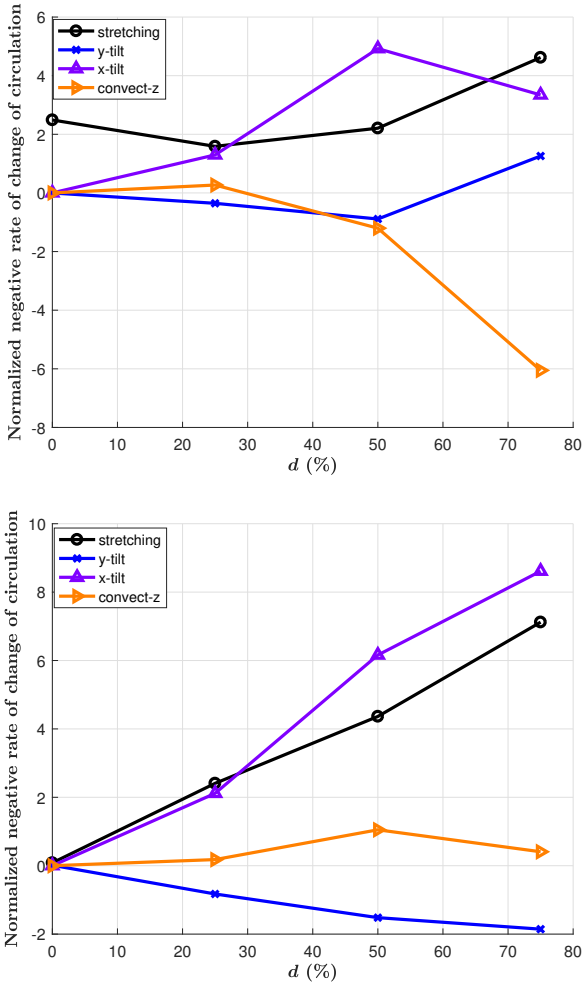


Figure 26: Normalized Fluxes measured along the span at 40 and 80 percent stroke for $Re$ 225.

For **case 2 at Re 500**, as the $Re$ is increased we can see the stability of the the LEV is significantly affected as well. The vorticity transport also shows high levels of dispersion. The trends seen in $Re225$ are not necessarily repeated. The contributions of the tilting, and spanwise convection terms are far greater. For the symmetry plane it is interesting to see no significant force peaks at the detachment FN (see figure 26). The tilting terms although not significant do not cancel each other out. Their presence at the symmetry plane however is still important as no

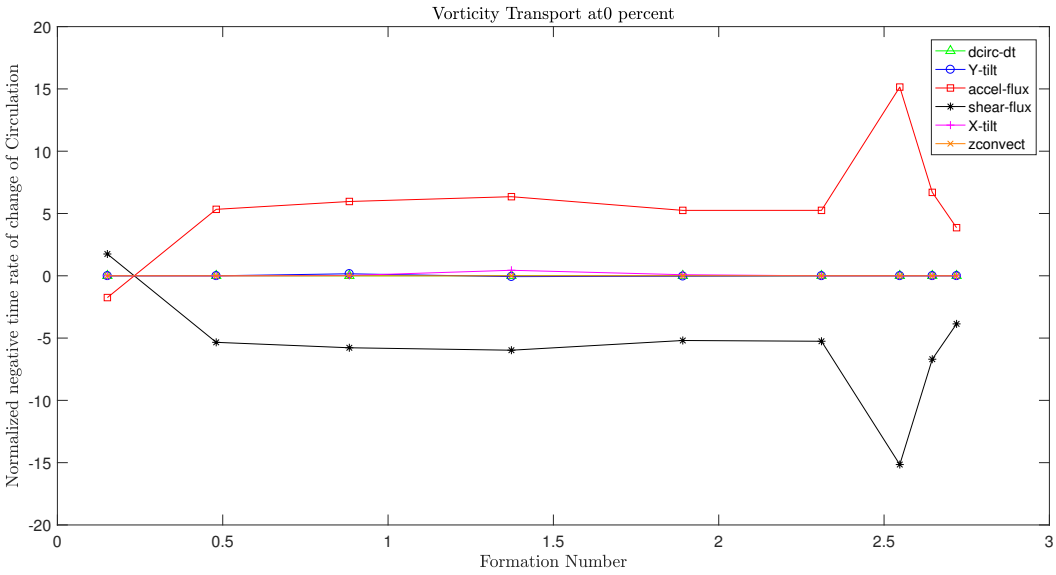


Figure 27: Normalized fluxes vs Formation number on a transformed plane at 0 percent of quarter perimeter for $Re$ 500.

deviation was expected from the symmetry plane for $Re$ 225. The magnitudes of the flux budgets compared to other planes is not that much lower as opposed to large changes in magnitudes for the $Re$ 255 case.

For $Re$ 500, at 50 percent plane, a large Y-tilt term that is seen before LEV detachment (see figure 27). Interestingly, while out-of-plane fluxes show high contribution to the vorticity transport before the first LEV break-off, their contributions significantly decrease in the lead up to the second LEV break off. We also notice another peculiarity in the tilting terms as they interchange between source and sink after the first LEV breakoff. The deviation in trends from lower $Re$ to higher $Re$ needs to be studied more as no conclusive observation can be made with just 2 simulations.

The vorticity transport results at 75 percent are quite intriguing (see figure 28). The graph deviates from the observation made for case 1 that the individual fluxes would follow the same trends as we move from root to tip. In-fact the plot at

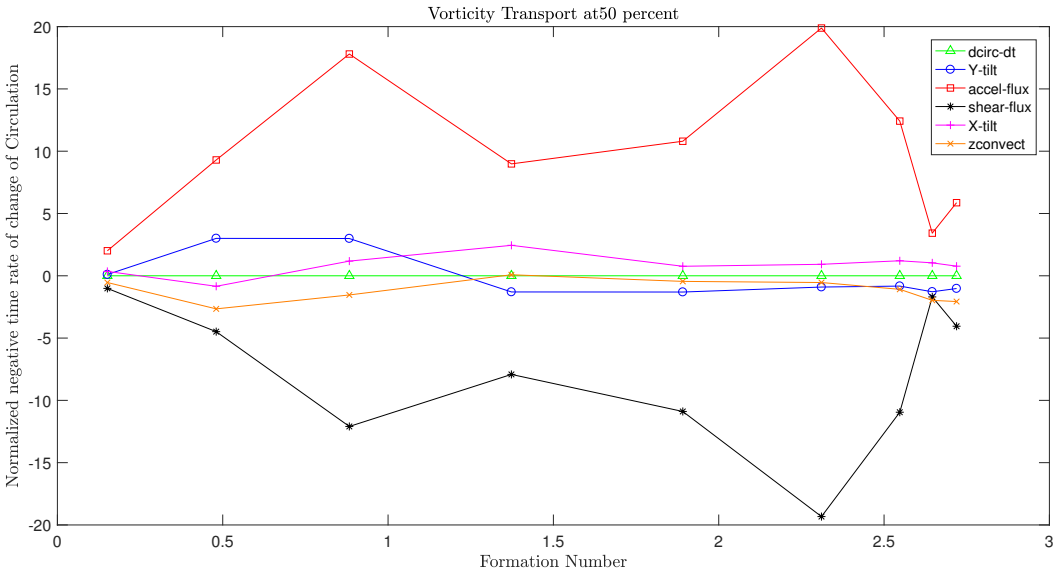


Figure 28: Normalized fluxes vs Formation number on a transformed plane at 50 percent of quarter perimeter for $Re$ 500.

75 percent plane for $Re$ 500 shows more similarity to the vorticity transport at 75 percent plane for $Re$ 225 than to the vorticty transport seen at other planes for the same $Re$. We do however see interchanging of tilting terms between source and sink, and a strong span wise convection occurring here.

The vorticity transport analysis carried out at the 4 different planes for the 2 cases of $Re$ give us an insight into the the contributions of the different fluxes involved in LEV formation and its stability. We see that for both cases, across the different planes, the shear flux is the dominant source term while the acceleration flux acts as the dominant sink term. Although not as dominant the out of plane fluxes are not negligible enough to be ignored and as seen in planar regions close to the tip contribute significantly to the over all flux budget.

The lower $Re$ case showed more predictable trends across the planes than the higher $Re$ case. It would be interesting to carry out further simulations to see if the

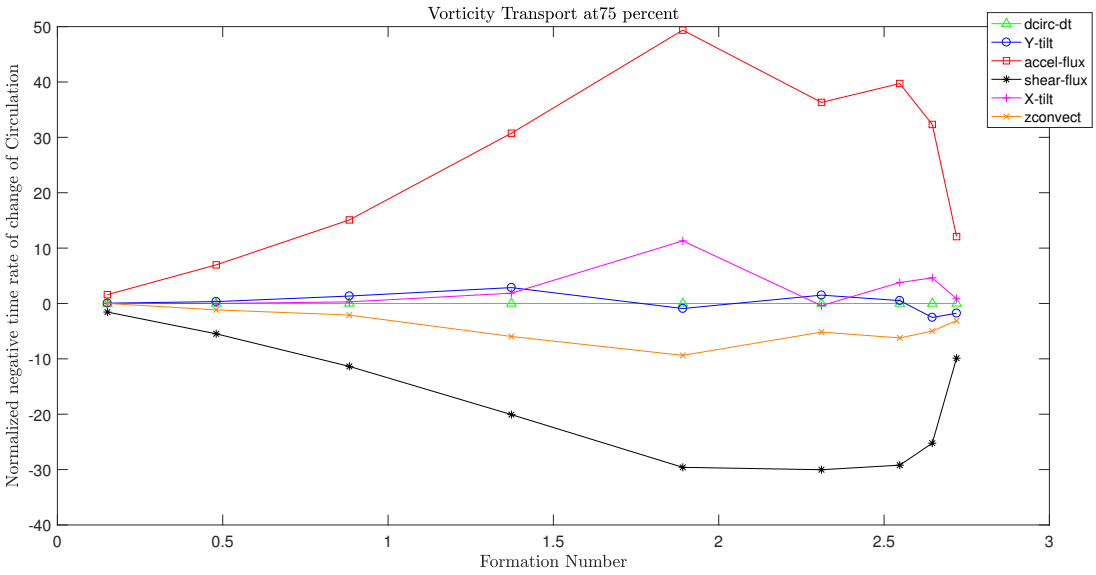


Figure 29: Normalized fluxes vs Formation number on a transformed plane at 75 percent of quarter perimeter for $Re$ 500.

interchanging of flux terms between source and sink, as seen for $Re$ 500, is a result of LEV instability or the cause of it. The trends seen for both cases of $Re$ Reinforces the observation that the geometry plays an important role in flux contributions especially at the tips where curvature increases drastically.

# 6. Conclusions and Future Work

The results of the numerical analysis conducted on an elliptic flat plate in hover has given us a good insight into LEV formation, and the effects of $Re$ on its stability. from both cases, the max LEV stability is observed at $Re$ 225, which is within the range of $Re$ seen in natural fliers with comparable wing size and geometry ($Re$ 190-225). Analyzing the formation number for its robustness as a non dimensional parameter leads us to conclude that further simulations must be carried out. The original definition clearly does not seem to hold, with a change in frequency yielding different formation numbers. However, the formation number is seen to be the same for both rectangular and elliptic flat plates at $Re$ 225, indicating that the LEV stability could be dependent on $Re$ or other parameters and not geometry. It is also seen that although individual planes show different LEV circulation values, for all the given values of $Re$, the overall LEV detachment occurs at the same time. To further study the 3-Dimensional nature of LEV formation we analyzed the vorticity transport equation and the contributions of various fluxes. The major source and sink terms are the shear flux and acceleration flux respectively. However, we also see that as we move away from the wing root the contributions of the out of plane fluxes increases and their contributions to the over all vorticity transport become significant, especially around the point of max circulation and LEV break off. This shows that geometrical features like curvature have an effect on vorticity transport.

## 6.2 Future Work

The results obtained and consequent observations we make point to several trends in LEV formation that need to studied more to fully understand them:

- The effect of $Re$ is clearly seen on LEV stability , we propose carrying out more simulations for different $Re$ around the 190 to 300 region to gain more insights into why natural fliers choose these ranges of flapping.
- Simulating different trajectories and find the effects on LEV formation.
- simulating different geometries closely matching wing geomertries of other natural fliers, to further understand the dependence or independence of LEV stability on wing geomtry.
- Test the Robustness of Formation Number. While our results point to the FN definition not being as robust as expected to reach a conclusive result more simulations must be conducted.
- Conduct a floquet stability analysis of the wake vortex.

# Appendix

*Re* 225

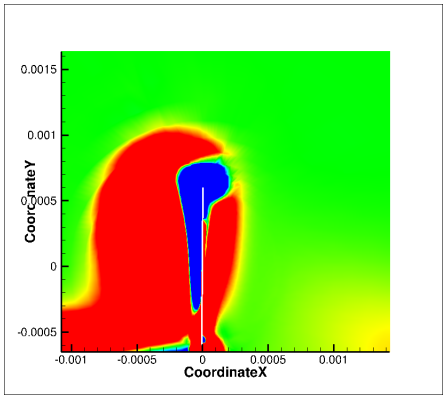


t=3000

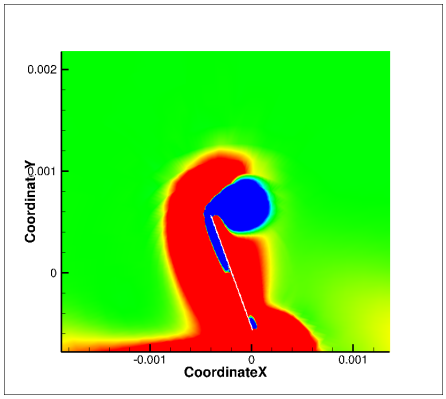


t=3050

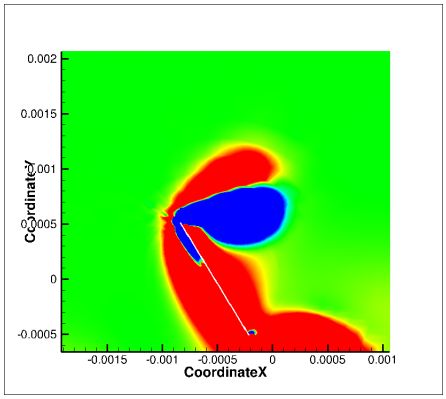


t=3100

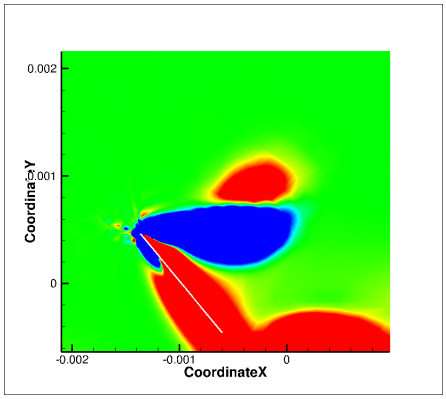


t=3150

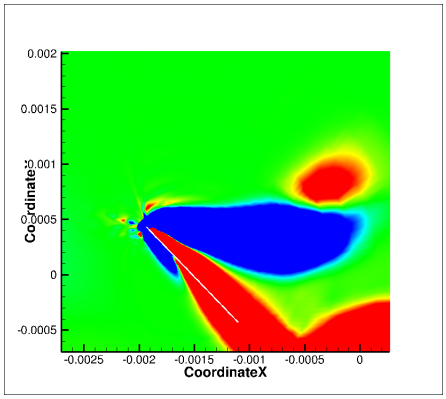


t=3200

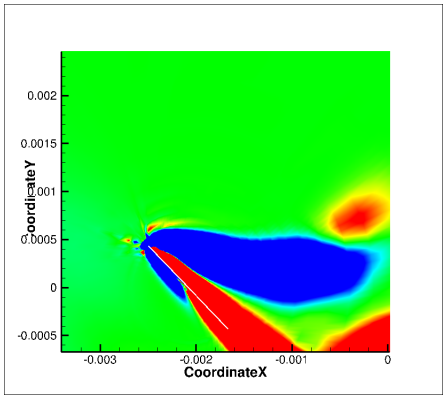


t=3250

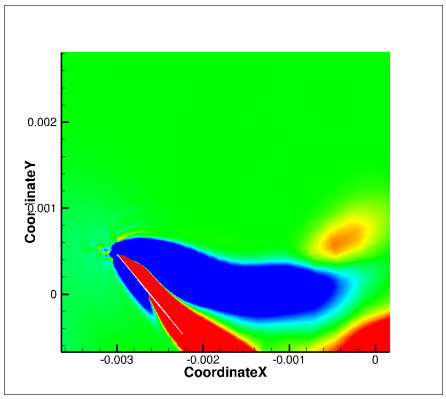


t=3300

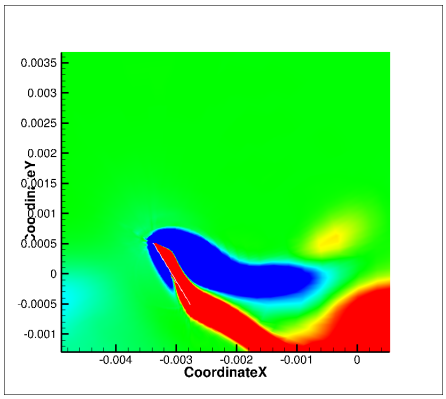


t=3350

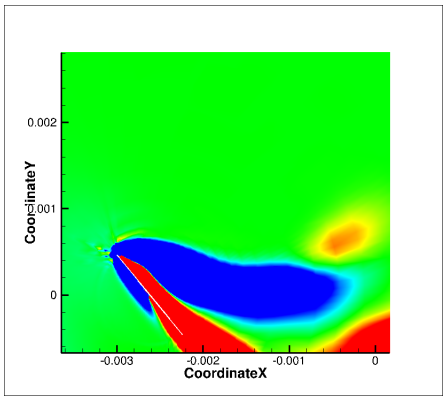


t=3400

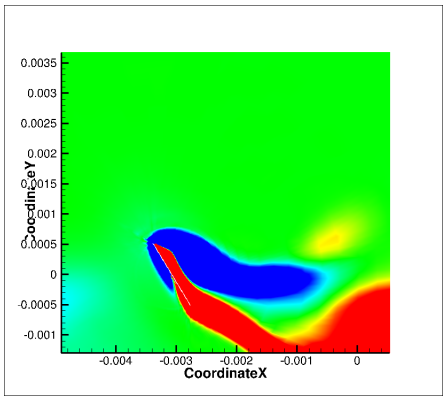


t=3450

$Re$ 500

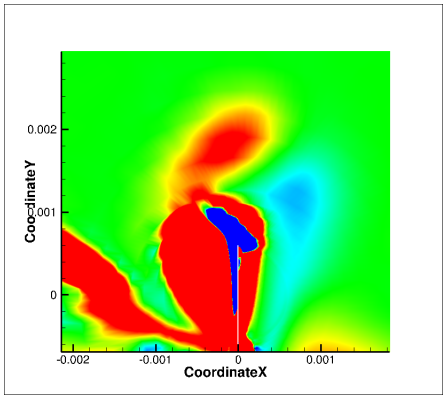


t=3000

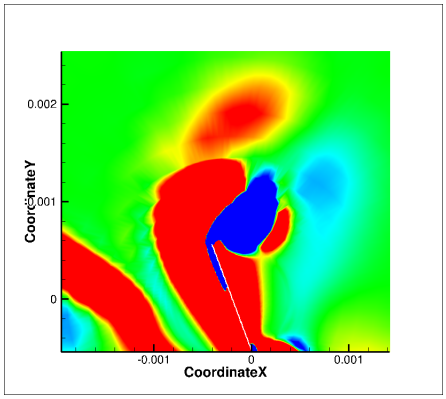


t=3050

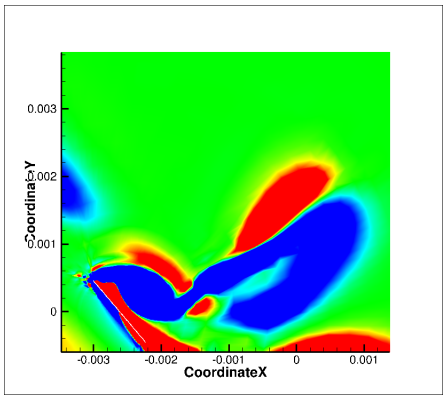


t=3100

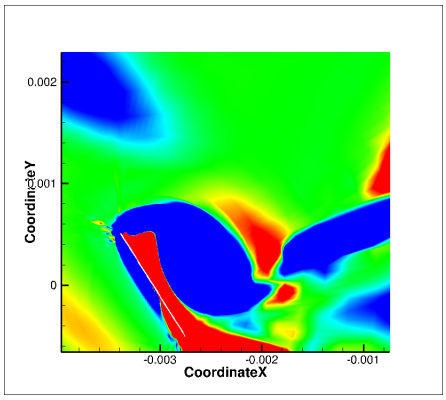


t=3150

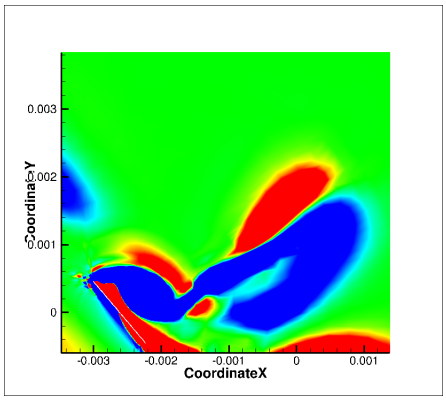


t=3200

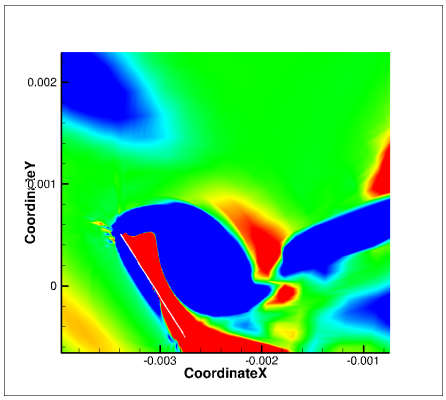


t=3250

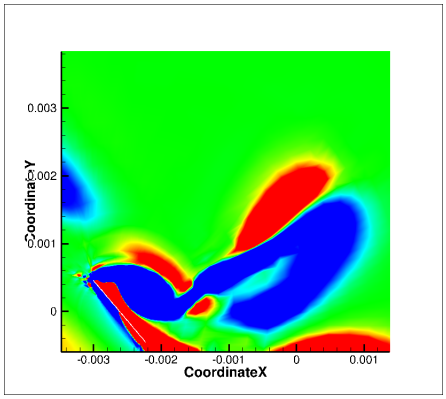


t=3300

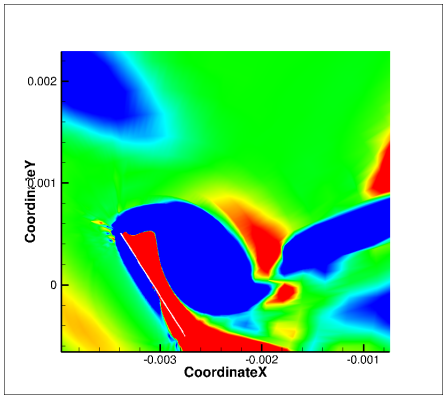


t=3350

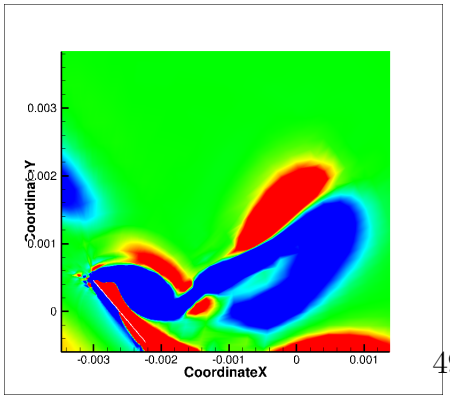


t=3400

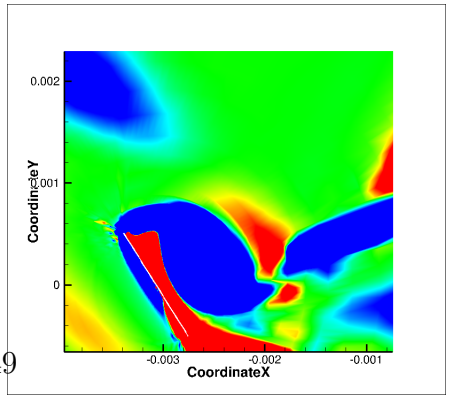


t=3450

Bibliography

[1] MFM Osborne. Aerodynamics of flapping flight with application to insects. *Journal of Experimental Biology*, 28(2):221–245, 1951.

[2] Sanjay P Sane. The aerodynamics of insect flight. *Journal of experimental biology*, 206(23):4191–4208, 2003.

[3] Douglas R Warrick, Bret W Tobalske, and Donald R Powers. Aerodynamics of the hovering hummingbird. *Nature*, 435(7045):1094–1097, 2005.

[4] David Lentink and Michael H Dickinson. Rotational accelerations stabilize leading edge vortices on revolving fly wings. *Journal of Experimental Biology*, 212 (16):2705–2719, 2009.

[5] Morteza Gharib, Edmond Rambod, and Karim Shariff. A universal time scale for vortex ring formation. *Journal of Fluid Mechanics*, 360:121–140, 1998.

[6] John O Dabiri and Morteza Gharib. Delay of vortex ring pinchoff by an imposed bulk counterflow. *Physics of Fluids*, 16(4):L28–L30, 2004.

[7] Azar Eslam Panah, James M Akkala, and James HJ Buchholz. Vorticity transport and the leading-edge vortex of a plunging airfoil. *Experiments in Fluids*, 56 (8):160, 2015.

[8] Siddarth Chintamani, Alok A Rege, Brian H Dennis, and Kamesh Subbarao. Three-dimensional effects in the wake vortex formation of flapping flat plate in hover. In *54th AIAA Aerospace Sciences Meeting*, page 1067, 2016.

[9] Robert C Michelson and Steven Reece. Update on flapping wing micro air vehicle research-ongoing work to develop a flapping wing, crawling entomopter. In *13th Bristol International RPV/UAV Systems Conference Proceedings, Bristol England*, volume 30, pages 30–1, 1998.

[10] Paul S Krueger, John O Dabiri, and Morteza Gharib. The formation number of vortex rings formed in uniform background co-flow. *Journal of Fluid Mechanics*, 556:147–166, 2006.

[11] Michele Milano and Morteza Gharib. Uncovering the physics of flapping flat plates with artificial evolution. *Journal of Fluid Mechanics*, 534:403–409, 2005.

[12] Craig J Wojcik and James HJ Buchholz. Vorticity transport in the leading-edge vortex on a rotating blade. *Journal of Fluid Mechanics*, 743:249–261, 2014.

[13] CP Ellington. The aerodynamics of hovering insect flight. i. the quasi-steady analysis. *Philosophical Transactions of the Royal Society of London B: Biological Sciences*, 305(1122):1–15, 1984.

[14] Torkel Weis-Fogh. Energetics of hovering flight in hummingbirds and in drosophila. *Journal of Experimental Biology*, 56(1):79–104, 1972.

[15] Torkel Weis-Fogh. Quick estimates of flight fitness in hovering animals, including novel mechanisms for lift production. *Journal of experimental Biology*, 59(1): 169–230, 1973.

[16] Coen Van Den Berg and Charles P Ellington. The three–dimensional leading–edge vortex of a hoveringmodel hawkmoth. *Philosophical Transactions of the Royal Society of London B: Biological Sciences*, 352(1351):329–340, 1997.

[17] Steven N Fry, Rosalyn Sayaman, and Michael H Dickinson. The aerodynamics of free-flight maneuvers in drosophila. *Science*, 300(5618):495–498, 2003.

[18] C Poelma, WB Dickson, and MH Dickinson. Time-resolved reconstruction of the full velocity field around a dynamically-scaled flapping wing. *Experiments in Fluids*, 41(2):213–225, 2006.

[19] Z Jane Wang, James M Birch, and Michael H Dickinson. Unsteady forces and flows in low reynolds number hovering flight: two-dimensional computations vs robotic wing experiments. *Journal of Experimental Biology*, 207(3):449–460, 2004.

[20] FT Muijres, LC Johansson, Ryan Barfield, Marta Wolf, GR Spedding, and Anders Hedenström. Leading-edge vortex improves lift in slow-flying bats. *Science*, 319(5867):1250–1253, 2008.

[21] Clara OFarrell and John O Dabiri. Pinch-off of non-axisymmetric vortex rings. *Journal of Fluid Mechanics*, 740:61–96, 2014.

[22] Matthew J Ringuette, Michele Milano, and Morteza Gharib. Role of the tip vortex in the force generation of low-aspect-ratio normal flat plates. *Journal of Fluid Mechanics*, 581:453–468, 2007.

[23] Daegyoum Kim and Morteza Gharib. Flexibility effects on vortex formation of translating plates. *Journal of Fluid Mechanics*, 677:255–271, 2011.

[24] Bram Van Leer. Towards the ultimate conservative difference scheme. v. a second-order sequel to godunov's method. *Journal of computational Physics*, 32(1):101–136, 1979.

[25] Sergei Konstantinovich Godunov. A difference method for numerical calculation of discontinuous solutions of the equations of hydrodynamics. *Matematicheskii Sbornik*, 89(3):271–306, 1959.